Contents lists available at ScienceDirect

Precambrian Research

Source of gold in Neoarchean orogenic-type deposits in the North Atlantic Craton, Greenland: Insights for a proto-source of gold in sub-seafloor hydrothermal arsenopyrite in the Mesoarchean

N.J. Saintilan[a,*], D. Selby[a,b], J.W. Hughes[a,c], D.M. Schlatter[d], J. Kolb[e], A. Boyce[f]

[a] Department of Earth Sciences, University of Durham, Durham DH1 3LE, United Kingdom
[b] State Key Laboratory of Geological Processes and Mineral Resources, School of Earth Resources, China University of Geosciences, Wuhan, China
[c] Bluejay Mining Plc, 2nd Floor, 7-9 Swallow Street, London W1B 4DE, United Kingdom
[d] Helvetica Exploration Services GmbH, Carl-Spitteler-Strasse 100, 8053 Zürich, Switzerland
[e] Institute of Applied Geosciences, Department of Geochemistry and Economic Geology, Karlsruhe Institute of Technology, Adenauerring 20b, 76131 Karlsruhe, Germany
[f] Isotope Geoscience Unit, SUERC, Rankine Avenue, East Kilbride, Glasgow G75 0QF, United Kingdom

ABSTRACT

Given that gold (Au) mostly remained in the incipient Earth mantle until ca. 3.9–3.8 Ga, a "proto-source" of gold may have been present in the dominantly mafic crust precursor born through first-stage melting of the early Earth mantle. In south-westernmost Greenland, a fragment of the North Atlantic Craton is characterised by greenstone belts comprising mafic volcanic and magmatic rocks, and harzburgite cumulates that were emplaced at ca. < 3.19–3.01 Ga (e.g., Tartoq greenstone belt). Here, combining detailed sulphide petrography with rhenium-osmium-sulphur (Re-Os-S) isotope geochemistry of individual mineral separates of arsenopyrite from gold-sulphide mineralised shear zones, we pinpoint the precipitation of ca. 3.18–3.13 Ga (Re-Os model ages) hydrothermal arsenopyrite associated and coeval with arc-related magmatism of the Tartoq Group. We consider sub-seafloor hydrothermal alteration of the oceanic crust and magmatic activity to have supplied arsenic (As), Re, and Au, to result in the precipitation of the ca. 3.18–3.13 Ga arsenopyrite with primary invisible gold. Additionally, in major shear zones in a rigid juvenile continental crust, retrograde greenschist-facies metamorphism overprinted the ca. > 3.0 Ga prograde amphibolite-facies metamorphic assemblages and caused local dissolution of arsenopyrite. During this retrograde tectono-metamorphic stage, in gold-rich shear zones, the Re-Os geochronometer in arsenopyrite was reset to a Neoarchean age while invisible gold was liberated and deposited as free gold with 2.66 Ga pyrite (Re-Os isochron ages). The initial Os isotope ratios of Neoarchean arsenopyrite ($^{187}Os/^{188}Os_i$ = 0.13 ± 0.02) and gold-bearing pyrite (0.12 ± 0.02) overlap with the estimated $^{187}Os/^{188}Os$ ratio of the Mesoarchean mantle (0.11 ± 0.01) and preclude contribution of radiogenic crustal Os from evolved lithologies in the accretionary arc complex, but instead, favour a local contribution in Os from basaltic rocks and serpentinised harzburgite protoliths by metamorphic fluids. Thus, the ca. 2.66 Ga lode gold mineralisation identified in the North Atlantic Craton may illustrate a gold endowment in shear zones in Earth's stabilizing continental crust at the time of the 2.75–2.55 Ga Global Gold Event, through metamorphic upgrading of bulk gold which had originally been extracted from the Mesoarchean mantle and concentrated in hydrothermal arsenopyrite deposits in oceanic crust beneath the overall reduced Mesoarchean ocean.

1. Introduction

On Earth, the abundance of a given element (e.g., gold, Au), for example in the continental crust, may be either (1) the result of its partitioning from the internal material as a result of the differentiation of Earth's bulk composition and reorganization of its interior structure through the impact of core-mantle-plate geodynamics (Shahar et al.,

2019), or, (2) the result of a preserved extra-terrestrial input supplied over a prolonged period of time (e.g., iridium enrichment in the cap carbonate sequences – an outcome from the demise of the Cryogenian Snowball Earth; Bodiselitsch et al., 2005). In fact, unlike osmium and iridium, which were sequestered into the core in the incipient Earth between 4.51 and > 3.90 Ga and replenished by the late veneer at ca. 3.90 to 3.80 Ga (Fig. 1A & B; Brenan and McDonough, 2009; Willbold

---

* Corresponding author at: Institute of Geochemistry and Petrology, Department of Earth Sciences, ETH Zürich, Clausiusstraße 25, 8092 Zürich, Switzerland.
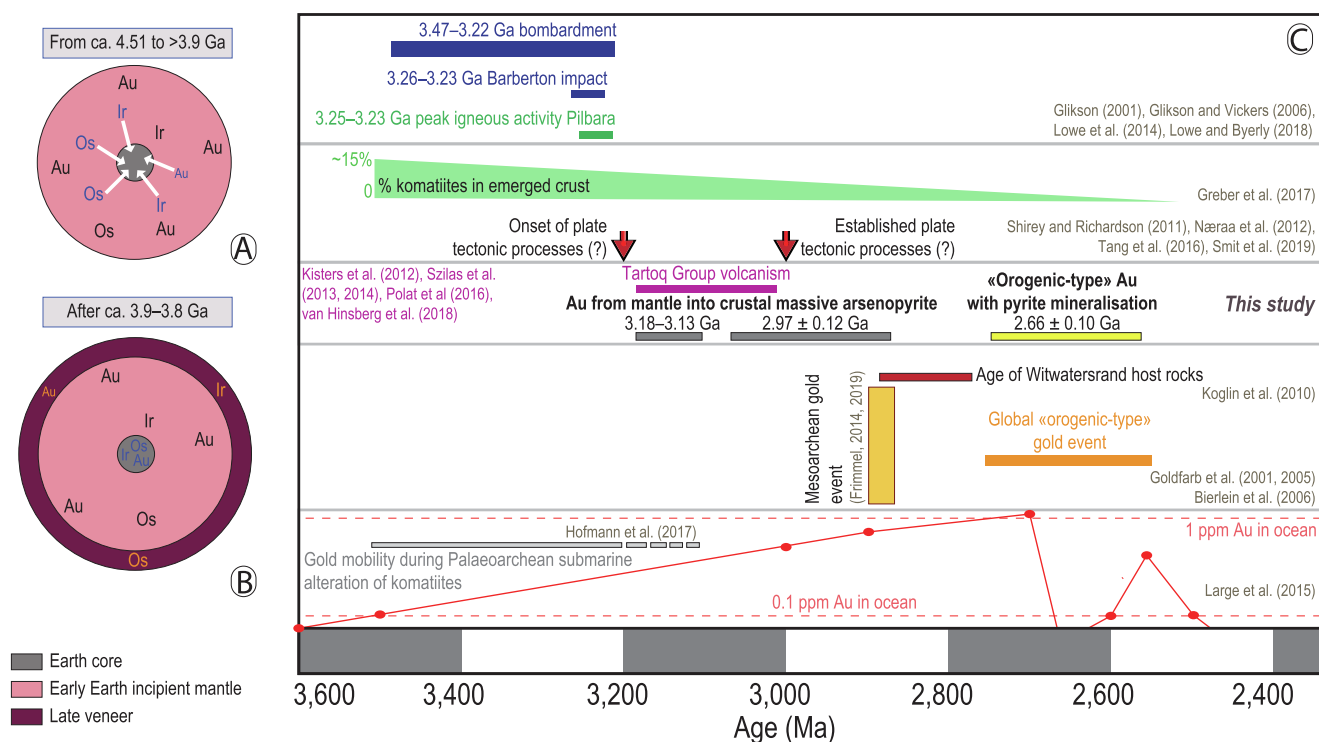 *E-mail address:* nicolas.saintilan@erdw.ethz.ch (N.J. Saintilan).

Fig. 1. Summary of what is currently known regarding the distribution of gold in Earth structural layers starting from the Hadean through to the Archean (see text for details regarding Fig. 1A, B, and C). Following the line of research of Glikson (2001), Glikson and Vickers (2006) established a connection between the 3.26–3.24 Ga Barberton bolide impact and the consequent 3.26–3.23 Ga peak in igneous activity in the Pilbara area (Glikson and Vickers, 2006). In light of this work and the recent review of the Late Heavy Bombardment by Lowe and Byerly (2018), we hypothesize that the Mesoarchean gold proto-source in the oceanic crust, for which the Tartoq greenstone belt is representative, might be one expression of the geodynamic, tectonic and magmatic consequences of a recognized late stage for an extended Late Heavy Bombardment between 3.47 and 3.22 Ga (Lowe and Byerly, 2018). The conversion of the kinetic energy of bolide impactors into calorific energy transferred to the early Earth crust and mantle could have caused the stripping of gold from the Mesoarchean mantle and deeply influenced the hydrothermal alteration in a geothermally active oceanic crust. (See above-mentioned references for further information.)

et al., 2011; Barboni et al., 2017), gold mostly remained in the material that would differentiate into the young Earth's mantle (Fig. 1B; Brenan and McDonough, 2009). Therefore, it is critical to understand how and when a "proto-source" of gold was extracted from the Earth mantle and made available into the mafic crust precursor through first-stage melting of the mantle in the Archean. Second-stage melting of this mafic precursor, which produced more felsic rocks, would re-distribute gold in a more mature crust comprising tonalite-trondhjemite-granodiorite (TTG) bodies and granite-greenstone belts (Shirey and Richardson, 2011; Reimink et al., 2016; O'Neil and Carlson, 2017; O'Neil et al., 2019; Johnson et al., 2019; Laurent et al., 2020).

Previous benchmark studies have suggested that an overwhelming proportion of the gold in present-day Earth's continental crust may have been concentrated at ca. 2.9–2.7 Ga at the time of the unique interplay between atmospheric, hydrodynamical and biological conditions concurring to the formation of palaeoplacers in the Mesoarchean (i.e., the "Mesoarchean gold event"; Frimmel, 2014, 2018; Heinrich, 2015; Fig. 1C). Then, to explain the distribution of gold deposits in the Earth crust through geological times (Groves et al., 2005; Goldfarb et al., 2001, 2010; Frimmel, 2018), it was proposed that the ca. 2.9–2.7 Ga gold source in Earth's crust was redistributed in an array of ore deposit styles that could only be generated by the repeated action of plate tectonics (possibly starting from at ca. 3.2 to 3.0 Ga; Shirey and Richardson, 2011; Næraa et al., 2012; Tang et al., 2016; Smit et al., 2019) and the establishment from ca. 2.7 Ga of a continental crust rigid enough to be able to record strong regional deformation fabrics (Hawkesworth et al., 2019).

Here, we take a step back and investigate the origin and nature of a "proto-source" of gold complementary to the ca. 2.9–2.7 Ga gold source created during the "Mesoarchean gold event" (Frimmel, 2019).

Building on previous research for the Paleoarchean, we explore the concept envisaging that a "pool" of gold existed in the geothermally active mafic crust of the Mesoarchean Earth (Large et al., 2015; Hofmann et al., 2017). Thus, we first present a review on the pool of gold during the Paleoarchean (Large et al., 2015; Hofmann et al., 2017) and the origin of Mesoarchean palaeoplacers (Frimmel, 2014, 2018; Heinrich, 2015) to piece together what is currently known about the endowment of the crust in gold from the Paleoarchean until the Mesoarchean gold event.

In contrast to the low fertility of Paleoarchean granite-greenstone belts for lode gold deposits (also referred as "orogenic gold deposits") and given a sharp decrease in the abundance of komatiites within the Earth's crust from ca. 3.2 Ga (Fig. 1C; Greber et al., 2017), we postulate that the Mesoarchean mafic crust could have retained its gold and been a fertile source for Neoarchean structurally-controlled lode gold deposits in Mesoarchean greenstone belts. Examples of such structurally-controlled gold deposits of Neoarchean age, which are coeval with amphibolite-facies metamorphism of mafic protoliths in greenstone belts (e.g., ca. 2.64 Ga gold-bearing arsenopyrite mineralisation at Storø; Scherstén et al., 2012), exist in the Greenland fragment of the North Atlantic Craton (GNAC; inset in Fig. 2A).

In the Tartoq District within the GNAC (Fig. 2A), a complex patchwork of mafic crustal rocks and protoliths of serpentinised harzburgite formed at ca. < 3.19–3.01 Ga (Szilas et al., 2013, 2014; Polat et al., 2016; van Hinsberg et al., 2018). Several shear zones affect those rocks and host gold mineralisation (Appel and Secher, 1984; Petersen, 1991; Kisters et al., 2012; Kolb et al., 2013), in particular in the Nuuluk area in the Tartoq greenstone belt (Fig. 2A and B), where gold is associated with massive arsenopyrite (FeAsS) and pyrite (FeS$_2$). Here, we contribute new evidence about the nature of crust-forming processes in
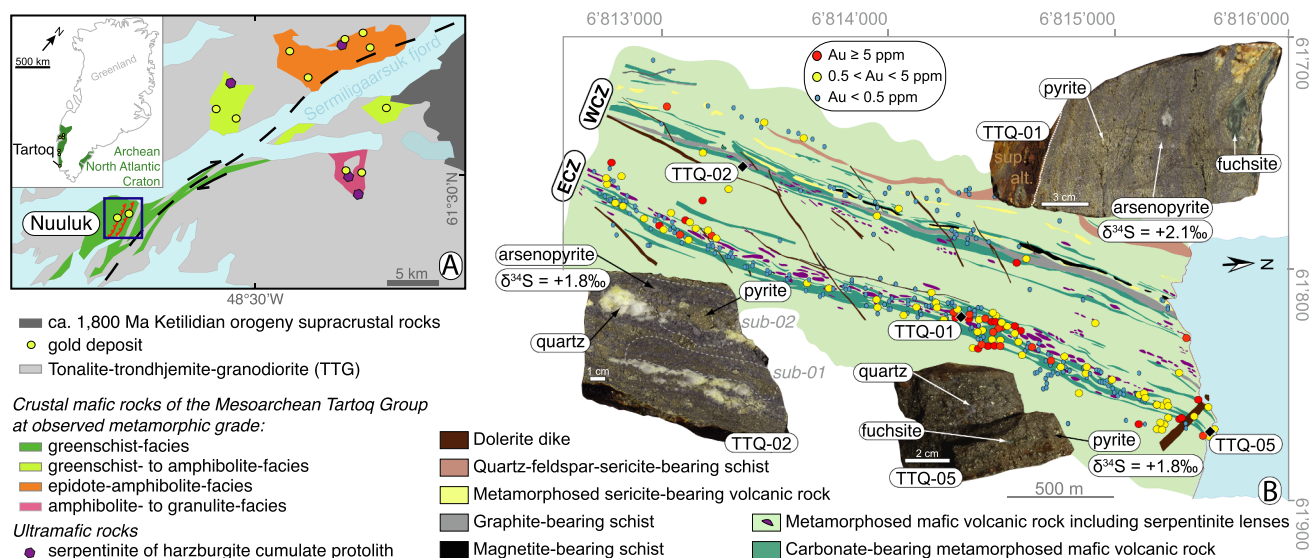
Fig. 2. The Tartoq greenstone belt and gold mineralisation in the Greenland fragment of the North Atlantic Craton (GNAC). (A) Geological and structural map of the Tartoq district after Petersen (1991). Inset: Location of the GNAC and the main gold occurrences in southwestern Greenland after Kolb et al. (2013), (B) Geological map of the Nuuluk area in the Tartoq greenstone belt showing location of the gold-mineralised Western and Eastern Carbonate Zones (WCZ & ECZ, after Petersen (1991) and Szilas et al. (2013, 2014)). The photographs show the three samples selected for Re-Os-S isotope geochemistry studies. The whole-rock gold assays are after the database of Nanoq Resources Ltd. (publicly available in AEX Gold's NI-43-101 SRK Technical Report by Russill and Kellaway, 2017), and historic exploration data compiled by Kolb (2011). Abbreviation: sup. alt.: supergene alteration.

the Mesoarchean and the nature of a sink for gold extracted from the Mesoarchean mantle. To this end, we undertook detailed petrographic and paragenetic studies of the sulphide and gangue minerals, combined with rhenium-osmium-sulphur (Re-Os-S) isotope geochemistry of individual mineral separates of arsenopyrite and pyrite. Our work recognizes the existence of ca. < 3.18–3.00 Ga sub-seafloor, hydrothermal, gold-bearing, massive arsenopyrite proto-ores, from which gold was concentrated, probably, in the first "orogenic gold deposits" at ca. 2.66 Ga, thereby contributing to the ca. 2.75–2.55 Ga "Global Gold Event" in the incipient and stabilizing continental crust (Fig. 1C; Goldfarb et al., 2001, 2005; Bierlein et al., 2006; Frimmel, 2018).

2. Current understanding of the endowment of the crust in gold in the Paleoarchean and Mesoarchean

The bimodal felsic and mafic crust in Archean cratons may be the result of (1) a first-stage melting of the early mantle producing a mafic crustal precursor, and, (2) a second-stage melting of this mafic precursor yielding felsic rocks (O'Neil et al., 2019). In his model for the source of gold in palaeoplacers in the Mesoarchean (e.g., the giant Witwatersrand Basin), Frimmel (2014, 2019) explains that mass balance calculations exclude the sole contribution by auriferous vein deposits hosted by (Eo-?), Paleo- and Mesoarchean granite-greenstone belts in the hinterland of the Archean cratons. Instead a source of the gold in palaeoplacers is explained by the unique interplay of (i) atmospheric conditions, (ii) ocean and riverine water chemistry, (iii) atmospheric weathering driven by $pH_{2(g)}$ causing non-redox acidic dissolution of Fe(II)-species or reduction of Fe(III)-species (Hao et al., 2019), and (iv) evolution of life at ca. 2.9 Ga that triggered continent-wide leaching, transfer of gold to reduced seawater as $Au(HS)_2^-$ and, subsequent large-scale trapping of gold in and around coastal environments in the Mesoarchean (Heinrich, 2015; Large et al., 2015; Frimmel, 2019). This source of gold in seawater (Fig. 1C; Large et al., 2015; Hofmann et al., 2017) was readily explained by the extensive transfer of gold to the anoxic Paleoarchean ocean, with limited incorporation of gold into carbonaceous chert, as a result of low-temperature (< 150 °C) hydrothermal seafloor alteration and pervasive silicification of an

oceanic crust comprising large volumes of Paleoarchean komatiites with high MgO and naturally low Au contents (Anhaeusser et al., 1975; Brügmann et al., 1987; Greber et al., 2017; Hofmann et al., 2017).

3. Geology of the Tartoq greenstone belt

The GNAC is fringed by Paleoproterozoic orogenic belts to the north and south (Kolb et al., 2013 and references therein). Several > 3600 Ma to ca. 2550 Ma tectonic terranes or blocks of Archean rocks were involved in a major accretionary orogeny at ca. 2720–2700 Ma (Nutman and Friend, 2007; Kolb et al., 2012; Dziggel et al., 2014, 2017), with cratonisation concluding at ca. 2560 Ma (Friend et al., 1988, 1996; Nutman and Friend, 2007; Nutman et al., 1989, 2004). At the southwestern margin of the GNAC (inset in Fig. 2A), the greenstone belt comprising the Tartoq Group is found in six individual km-scale synclinal structures that all host several orogenic gold occurrences (Fig. 2A; Nielsen, 1976; Appel and Secher, 1984; Kolb et al., 2013; Steenfelt et al., 2016). The Mesoarchean Tartoq Group comprises mafic rocks with well-preserved primary volcanic and magmatic features (e.g., subaqueous lava flows including evidence of pillow lavas, volcanic breccias) together with serpentinites of harzburgite cumulate protoliths that originally formed by hydrous melting of a shallow mantle source (Szilas et al., 2013, 2014). These rocks are interpreted as remnant of a < 3190–3012 Ma Mesoarchean oceanic crust involved in an accretionary complex (Kisters et al., 2012; Szilas et al., 2013, 2014; Polat et al., 2016; van Hinsberg et al., 2018; Fig. 2A). Accretion and stacking of this hydrated oceanic crust resulted in the formation of ca. 3012–2993 Ma felsic mylonites in thrusts, and imbrication of the Tartoq Group rocks with voluminous TTGs as young as 2824 Ma (Nutman et al., 2004; Polat et al., 2016). These TTGs may have formed by the melting of thickened oceanic crust (Nagel et al., 2012; Hastie et al., 2016) in a "repeatedly-aborted subduction zone" setting (Kisters et al., 2012; Szilas et al., 2013, 2014; van Hinsberg et al., 2018). As a consequence of this tectonic evolution, in the Nuuluk part of the Tartoq greenstone belt, which is the focus of the present study, the Tartoq Group including lenses of ultramafic rocks was originally metamorphosed to the amphibolite facies (~580 °C, ~4.5 kbar) prior to and

possibly when imbricated into TTGs (Evans and King, 1993; Kisters et al., 2012; Szilas et al., 2014; van Hinsberg et al., 2018, van Hinsberg, pers. comm. 2019). Shear zones are characterised by localized greenschist-facies retrograde metamorphism that overprint the peak amphibolite-facies assemblage in the Nuuluk area (van Hinsberg et al., 2018). The shear zones (Fig. 2B) comprise an anastomosing network of auriferous quartz-ankerite ± pyrite veins, which either have an ankerite-chlorite-quartz-pyrite-pyrrhotite-chalcopyrite-tennantite halo, or are locally walled by fuchsite ± tourmaline ± talc at the contact with serpentinite lenses (Evans and King, 1993; Kolb et al., 2013; van Hinsberg et al., 2018). Tourmaline thermometry and the retrograde assemblage of chlorite-albite-epidote-titanite-calcite in the mafic rocks attest to conditions of 380 ± 50 °C at a pressure < 2 kbar (~4 km depth; van Hinsberg et al., 2018).

Two 25-m-wide and ca. 5-km-long shear zones (i.e., the gold-rich Eastern and gold-poorer Western Carbonate Zones – ECZ & WCZ, Fig. 2B), which lie 500 m apart and are located ca. 100–200 m into the footwall of a major thrust zone (King, 1985; Evans and King, 1993; Kolb, 2011; Kolb et al., 2013; Steenfelt et al., 2016), host gold mineralisation found in three assemblages: (type 1) as 5–20 μm anhedral grains in arsenopyrite and pyrite (or in fractures in those minerals) in massive sulphide layers, in particular in the gold-rich ECZ (Evans and King, 1993; up to 20 ppm Au); (type 2) in discordant, pinch-and-swell veins composed of fine-grained quartz-ankerite veins with euhedral pyrite, which may cut across the massive arsenopyrite bodies and, in places were cemented by syn-tectonic fuchsite during an episode of vein re-opening (Appel and Secher, 1984; Evans and King, 1993; up to 106 ppm Au); (type 3) in tennantite ($Cu_{12}As_4S_{13}$)-bearing veins or in chalcopyrite ($CuFeS_2$)-quartz veins (Appel and Secher, 1984; Evans and King, 1993; Kolb, 2011; Kolb et al., 2013). The host rocks in the immediate vicinity of mineralisation comprise ankerite, chlorite, quartz and fuchsite, whereas carbonate, chlorite, tourmaline, and pyrite dominate away from the mineralised zones. The arsenopyrite-pyrite layers were interpreted as submarine exhalative in origin ("proto-ore") whereas the origin of chalcopyrite and tennantite was invoked as being related to an alteration of the primary massive sulphide layers during metamorphism (Appel and Secher, 1984).

4. Methods

4.1. Production of mineral separates of individual sulphide/sulpharsenide species

The protocol utilised in the present study to obtain mineral separates of individual sulphide species is described in detail in a companion method article entitled "Mineral separation protocol for accurate and precise rhenium-osmium (Re-Os) geochronology and sulphur isotope composition of individual sulphide species" and published in MethodX.

4.2. Re-Os isotope geochemistry

Following sulphide petrography and mineral separation, Re-Os isotope geochemistry of arsenopyrite and pyrite were carried out on samples TTQ-01, TTQ-02 and TTQ-05. For each analysis, between 188 and 530 mg of sulphide (arsenopyrite or pyrite) mineral separate were weighed and transferred into a thick-walled borosilicate Carius tube (Shirey and Walker, 1995). Each sulphide aliquot was dissolved in inverse Aqua Regia (~3 mL of 11 N HCl and ~6 mL 16 N HNO_3) with a known amount of "^{185}Re + ^{190}Os spike" solution or "^{185}Re + common Os spike" solution at 210 °C for 24 h (Laboratory for Sulphide and Source Rock Geochemistry and Geochronology in the Durham Geochemistry Centre, Durham University, UK; Selby et al., 2009). The "^{185}Re + common Os spike" solution was used for arsenopyrite mineral separates identified to being bereft of common Os following analysis using the "^{185}Re + ^{190}Os spike" solution (Table 1). The Re-Os

laboratory protocol used in the present work is described in full in Selby et al. (2009). The Re and Os isotopic compositions were determined by negative thermal ionization mass spectrometry (N-TIMS) using a ThermoScientific Triton mass spectrometer at the Arthur Holmes Laboratory in the Durham Geochemistry Centre, Durham University, UK. Rhenium was measured as ReO_4^- in static mode on Faraday collectors, whereas Os was measured as OsO_3^- in peak-hopping mode on a SEM (Creaser et al., 1991; Völkening et al., 1991). Sulphide measurement quality was monitored by repeated measurements of in-house Re (125 pg aliquot – $^{185}Re/^{187}Re$ = 0.59892 ± 0.00203, n = 74) and Os (DROsS – 50 pg aliquot, $^{187}Os/^{188}Os$ = 0.160869 ± 0.000410, n = 100) standard solutions. Total procedural blanks for each set of samples are reported in Table 1. The analytical uncertainties result from full error propagation of weighing errors, spike calibration, standard measurements, mass spectrometry analyses and blanks. When using the "^{185}Re + ^{190}Os spike" solution, the Re-Os ages are determined through regression of Re-Os data in $^{187}Os/^{188}Os$ vs. $^{187}Re/^{188}Os$ space using 2σ level absolute uncertainties and the error correlation, rho, using Isoplot v 4.15 (Ludwig, 2011) with the ^{187}Re decay constant of Smoliar et al. (1996; $\lambda^{187}Re = 1.666e^{-11} \pm 5.165e^{-14} \ a^{-1}$). Those Re-Os ages are based on the computation of Model 1 isochrons. Alternatively, the other Re-Os ages are determined as model ages (t) for aliquots analysed using the "^{185}Re + common Os spike" solution by using the formula: t = ln [($^{187}Os*/^{187}Re$) + 1]/($\lambda^{187}Re$), where $^{187}Os*$ is the measured content of radiogenic ^{187}Os.

After preliminary Re tests to estimate the Re content in each sample, full Re-Os isotope geochemistry isotope procedures were carried out using appropriate volumes of the "^{185}Re + ^{190}Os" spike solution. For arsenopyrite aliquots of sample TTQ-02, considering the blank levels that we report (Table 1), no less than 84–89% of ^{188}Os (i.e., the normalizing isotope of the common Os fraction) was contributed by the blank. At those blank levels, for a range of assumed initial $^{187}Os/^{188}Os$ ratios of 0.11, 1, 5 or 10, the Os budget in those aliquots comprise 99.97–99.98% radiogenic ^{187}Os. Therefore, considering an Os budget comprising 100% radiogenic ^{187}Os, aliquots of arsenopyrite from sample TTQ-02 were spiked using the "^{185}Re + common Os spike". As such, individual more precise model ages could be determined for each aliquot in the way described above.

4.3. Sulphur isotopic composition of the arsenopyrite and pyrite mineral separates

The sulphur isotopic composition of the sulphide and sulpharsenide mineral species are combined with the Re-Os ages and the initial Os isotopic composition of those minerals, where available, to constrain the source(s) of Os and S. Approximately 5–10 mg of arsenopyrite or pyrite mineral separate was utilised for each isotopic analysis. Sulphides were analysed by standard techniques (Robinson and Kusakabe, 1975) at the Scottish Universities Environmental Research Centre – SUERC, Glasgow, UK. The liberated gases were analysed on a VG Isotech SIRA II mass spectrometer, and standard corrections applied to raw $\delta^{66}SO_2$ values to produce true $\delta^{34}S$. Repeat analyses of international and SUERC standards NBS-123, IAEA-S-3, and CP-1 gave $\delta^{34}S$ values of +17.1‰, −32‰ and −4.6‰ respectively, with a standard error of ± 0.3‰ during the execution of these samples. Data are reported in $\delta^{34}S$ notation as per mil (‰) variations from the Vienna Cañon Diablo Troilite (V-CDT) standard.

5. Results

5.1. Sulphide petrography and paragenetic sequence

The paragenetic sequence, which is valid for the massive sulphide bodies in both the ECZ and the WCZ, is presented in Fig. 3A. In the ECZ, euhedral to mostly subhedral, medium- to coarse-grained (< 4 mm) arsenopyrite forms a textural layering with subhedral to anhedral,

Table 1
Synopsis of the Re-Os-S isotope geochemistry data for arsenopyrite and pyrite at Nuuluk, Tartoq Greenstone Belt.

Preliminary full Re-Os isotope geochemistry procedure using the "185Re + 190Os" spike solution

Sample ID	Tectono-stratigraphic position	Mineral	Sample weight (mg)	Re (ppb)	±2σ	Total Os (ppt)	±2σ	192Os (ppt)	±2σ	187Os* (ppt)	±2σ	%187Os*	187Re (ppb)	±2σ	187Re/188Os	±2σ	187Os/188Os	±2σ	rho	% Re blank	%187Os blk	%188Os blk
TTQ-APY-02	WCZ	Arsenopyrite	393.50	1.648	0.006	45	0	0	0	45	2	99.97	1.036	0.004	509043	1649046	22138	71722	1.000	0.35	0.007	88.97
TTQ-APY-02	WCZ	Arsenopyrite	396.06	1.732	0.006	48	0	0	0	48	2	99.98	1.088	0.004	598631	2151686	26378	94820	1.000	0.34	0.004	84.33

Full Re-Os isotope geochemistry procedure using the "185Re + common Os" spike solution

Sample ID	Tectono-stratigraphic position	Mineral	Sample weight (mg)	Re (ppb)	±2σ	187Re (ppb)	±2σ	187Os (ppt)	±2σ	187Os/188Os	±2σ	Model age (Ma)	±2σ*	±2σ* (%)
TTQ-02-01-APY/01	WCZ	Arsenopyrite	411.90	1.509	0.014	0.949	0.009	51.7	1.0		0.4	3184	42	1.3%
TTQ-02-01-APY/02	WCZ	Arsenopyrite	520.99	1.528	0.011	0.960	0.007	51.5	1.1		0.3	3136	33	1.1%
TTQ-02-02-APY/01	WCZ	Arsenopyrite	498.01	2.115	0.085	1.330	0.054	67.4	1.4		0.3	2967	124	4.2%
TTQ-02-02-APY/02	WCZ	Arsenopyrite	528.92	2.204	0.089	1.385	0.056	68.3	1.3		0.3	2889	120	4.2%
TTQ-02-02-APY/03	WCZ	Arsenopyrite	290.82	2.263	0.024	1.422	0.015	73.1	2.4		0.8	3009	47	1.6%
TTQ-02-02-APY/04	WCZ	Arsenopyrite	510.27	2.588	0.104	1.627	0.065	78.3	1.4		0.4	2822	118	4.2%

Full Re-Os isotope geochemistry procedure using the "185Re + 190Os" spike solution

Sample ID	Tectono-stratigraphic position	Mineral	Sample weight (mg)	Re (ppt)	±2σ	Total Os (ppt)	±2σ	192Os (ppt)	±2σ	187Re/188Os	±2σ	187Os/188Os	±2σ	rho	% Re blank	%187Os blk	%188Os blk
TTQ-01-APY/01	ECZ	Arsenopyrite	416.39	430	2	114	2	42	2	20	1	1.0	0.1	0.699	1.28	0.14	0.17
TTQ-01-APY/01-duplicate	ECZ	Arsenopyrite	510.18	385	4	109	2	40	2	19	1	1.1	0.1	0.685	1.22	0.04	0.20
TTQ-01-APY/02	ECZ	Arsenopyrite	411.06	415	2	84	2	30	1	28	1	1.4	0.1	0.704	1.35	0.14	0.25
TTQ-01-APY/03	ECZ	Arsenopyrite	188.96	534	11	119	4	43	3	25	2	1.3	0.1	0.688	2.38	0.10	0.50
TTQ-01-APY/04	ECZ	Arsenopyrite	372.80	456	5	548	10	221	9	4.1	0.2	0.3	0.0	0.677	1.41	0.04	0.05
TTQ-05-PY/01	ECZ	Pyrite	331.15	585	2	70	3	22	2	53	4	2.4	0.3	0.707	1.19	0.14	0.41
TTQ-05-PY/02	ECZ	Pyrite	242.60	369	1	78	4	28	3	26	3	1.4	0.2	0.707	2.57	0.26	0.45
TTQ-05-PY/03	ECZ	Pyrite	363.87	311	5	834	29	341	28	1.8	0.1	0.2	0.0	0.706	2.03	0.10	0.02
TTQ-05-PY/04	ECZ	Pyrite	430.36	333	5	25	1	6.2	0.4	106	7	5.1	0.4	0.703	1.68	0.07	1.50
TTQ-05-PY/05	ECZ	Pyrite	370.89	364	4	19	1	3.5	0.3	208	19	9.5	1.1	0.730	1.78	0.08	3.12
TTQ-05-PY/06	ECZ	Pyrite	461.04	340	3	18	1	3.4	0.2	200	12	9.0	0.7	0.734	1.53	0.07	2.57
TTQ-02-PY/01	WCZ	Pyrite	425.95	960	4	45	3	5.1	0.1	378	5	20.8	0.3	0.701	0.56	0.05	1.39
TTQ-02-PY/02	WCZ	Pyrite	555.71	347	4	27	1	5.6	0.1	123	13	7.5	1.6	0.493	1.24	0.04	1.29
TTQ-02-PY/03	WCZ	Pyrite	521.77	351	4	16	1	1.5	0.1	480	34	26.9	2.4	0.790	1.31	0.05	5.29
TTQ-02-PY/04	WCZ	Pyrite	506.47	346	4	35	4	7.1	0.9	97	12	8.2	1.8	0.570	1.37	0.03	1.11
TTQ-02-PY/05	WCZ	Pyrite	442.41	275	4	20	2	2.1	0.1	158	17	10.9	2.2	0.506	1.65	0.05	2.20

Blank type	Os (ppt)	±2σ	Re (ppt)	±2σ	187Os/188Os	±2σ
Aqua Regia	0.08	0.02	2.3	0.06	0.80	0.2

Sample ID	Tectono-stratigraphic position	Mineral	δ34S (VCDT) ±0.2‰
TTQ-APY-02	WCZ	Arsenopyrite	1.8
TTQ-APY-01	ECZ	Arsenopyrite	2.1
TTQ-PY-05	ECZ	Pyrite	1.8

187Os*: radiogenic 187Os.

(*) uncertainty on the decay constant of 187Re is included.
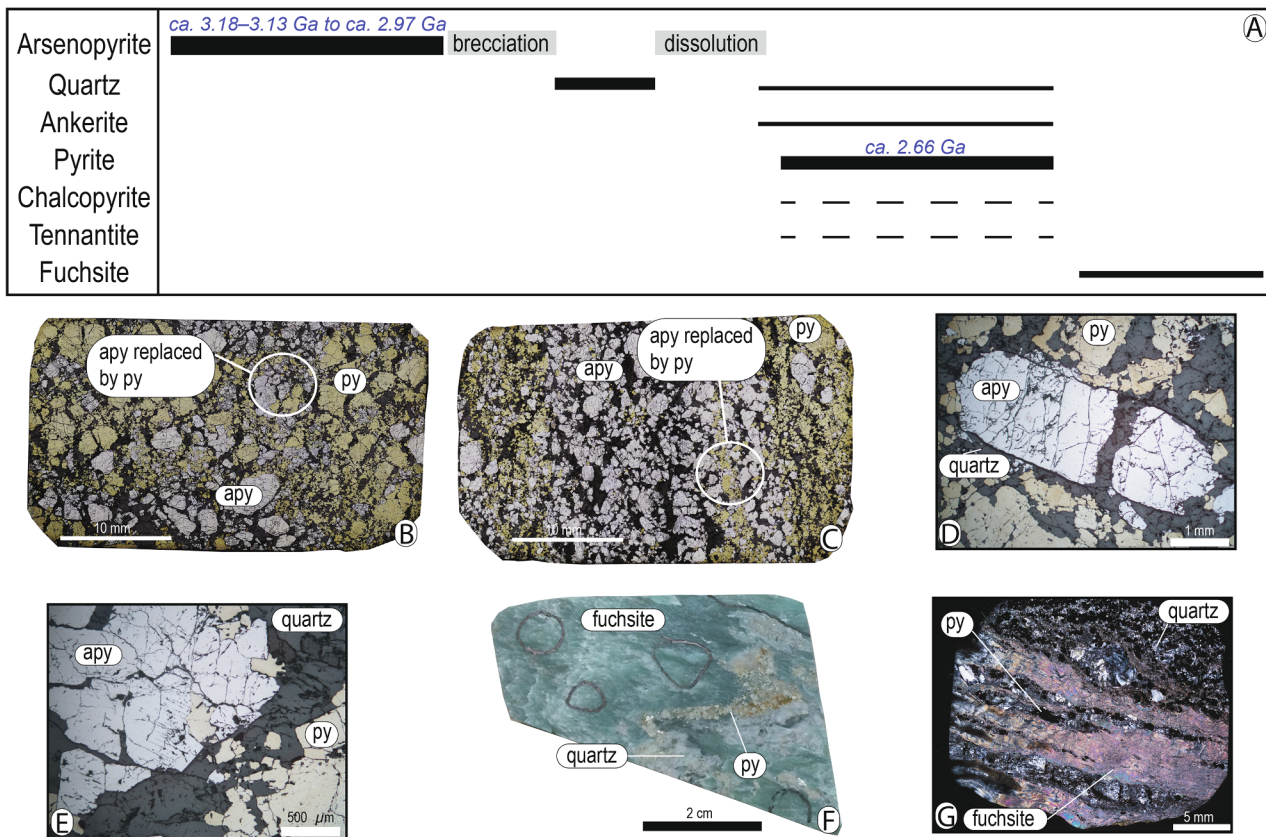
Fig. 3. A. Paragenetic sequence (i.e., relative timing) for the sulphide layers in the Western and Eastern Carbonate Zones (WCZ & ECZ) in the Nuuluk area of the Tartoq greenstone belt. The absolute Re-Os ages of arsenopyrite and pyrite determined in the present study are indicated in blue italics characters. B. Scan in reflected light microscopy of a polished section of sample TTQ-01 (ECZ). C. Scan in reflected light microscopy of a polished section of sample TTQ-02 (WCZ). D. Arsenopyrite brecciated and cemented by quartz in sample TTQ-01. E. Local dissolution of arsenopyrite and precipitation of pyrite at the locus of dissolution in sample TTQ-01. F. Quartz-pyrite veins in a fuchsite cement (ECZ). G. Details of anastomosing quartz-pyrite veins displaced by shear zones filled in with syn-tectonic fuchsite (ECZ).

coarse-grained (0.5 mm– < 4 mm) pyrite (TTQ-01, Fig. 3B). In the WCZ (Fig. 3C), euhedral to subhedral coarse-grained (ca. 1–2 mm) arseno-pyrite occurs between layers of younger medium- to coarse-grained subhedral to anhedral pyrite (ca. 0.25– > 2 mm; TTQ-02-sub-sample-01 in Fig. 2B). Locally, euhedral to subhedral arsenopyrite, which is associated with quartz and younger very coarse-grained pyrite (TTQ-02-sub-sample-02 in Fig. 2B), is very coarse-grained (> 2 mm).

Arsenopyrite exhibits localized features of weak recrystallization and intense brecciation prior to cementation by quartz (Fig. 3D). Arsenopyrite, which can be found as rounded or irregular inclusions in pyrite, was locally dissolved and partially replaced by pyrite (Fig. 3B, C, E). Locally, replacement of arsenopyrite by pyrite has resulted in the healing/destruction of fractures and brittle features within the arsenopyrite. Rare chalcopyrite and tennantite occur with pyrite. In the vicinity of lenses of serpentinites in the ECZ, open-space filling by fuchsite resulted in a pinch-and-swell pattern of pyrite-quartz veins (Fig. 3F, G).

5.2. Re-Os-S isotope geochemistry of monophasic mineral separates

In the WCZ, arsenopyrite ($\delta^{34}S$ = +1.8 ± 0.2‰ V-CDT, 2σ) is bereft of common Os and only contains radiogenic ^{187}Os ($^{187}Os^r$; Table 1). Two aliquots of the same mineral separate of euhedral to subhedral coarse-grained (ca. 1–2 mm) arsenopyrite in between layers of younger medium- to coarse-grained subhedral to anhedral pyrite (ca. 0.25– > 2.00 mm, sub-sample TTQ-02-01, "sub-01" in Fig. 2B) yield reproducible and precise Re-Os data (1.51–1.53 ppb Re and 51.5–51.7 ppt $^{187}Os^r$) with overlapping Mesoarchean Re-Os model ages of 3136 ± 33 Ma and 3184 ± 42 Ma (Fig. 4A; 1.1–1.3%, 2σ, with the

uncertainty including the ^{187}Re decay constant uncertainty; Smoliar et al., 1996). Four aliquots of the same mineral separate of euhedral to subhedral very coarse-grained (> 2 mm) arsenopyrite associated with quartz and younger very coarse-grained pyrite (sub-sample TTQ-02-02, "sub-02" in Fig. 2B) yield slightly less precise Re-Os data (2.12–2.59 ppb Re and 67.4–78.3 ppt $^{187}Os^r$) which yield overlapping Re-Os model ages of 2967 ± 124 Ma, 2889 ± 120 Ma, 3009 ± 47 Ma, 2822 ± 118 Ma and a weighted average of 2972 ± 120 Ma (4.0%, 2σ, Fig. 4A; n = 4, 95% confidence, mean square weighted deviates, MSWD = 3.6). Pyrite (n = 5, sample TTQ-02), which contains common Os, possesses lower Re and Os concentrations (0.275–0.960 ppb Re and 16–45 ppt total Os) than arsenopyrite in this sample. The regression of the Re-Os data of five pyrite aliquots from this sample, with a limited range in $^{187}Re/^{188}Os$ values (4–34), but positively correlated with the significantly radiogenic $^{187}Os/^{188}Os$ compositions (7.5–26.9), yields an imprecise Mesoarchean–Neoarchean Re-Os isochron age of 2860 ± 220 Ma (Fig. 4B; 2σ, Model 1 isochron; MSWD = 2.2, initial $^{187}Os/^{188}Os$ (Os$_i$) ratio = 2.4 ± 1.3).

Unlike arsenopyrite in the WCZ, arsenopyrite from the ECZ (sample TTQ-01; $\delta^{34}S$ = +2.1 ± 0.2‰) has lower Re concentrations (385–534 ppt) and contains common Os (for which a best approximation is given by the ^{192}Os contents of 30–221 ppt, ca. 35–40% of the total Os contents of 84–548 ppt). The regression of the Re-Os data of the four arsenopyrite aliquots, with a limited range in $^{187}Re/^{188}Os$ values (4–28), but positively correlated with the low to moderately radiogenic $^{187}Os/^{188}Os$ compositions (0.3–1.4), yielded a Neoarchean Re-Os isochron age of 2608 ± 108 Ma (Fig. 4C; 2σ, Model 1 isochron; MSWD = 3.0, initial $^{187}Os/^{188}Os$ (Os$_i$) ratio = 0.13 ± 0.02).
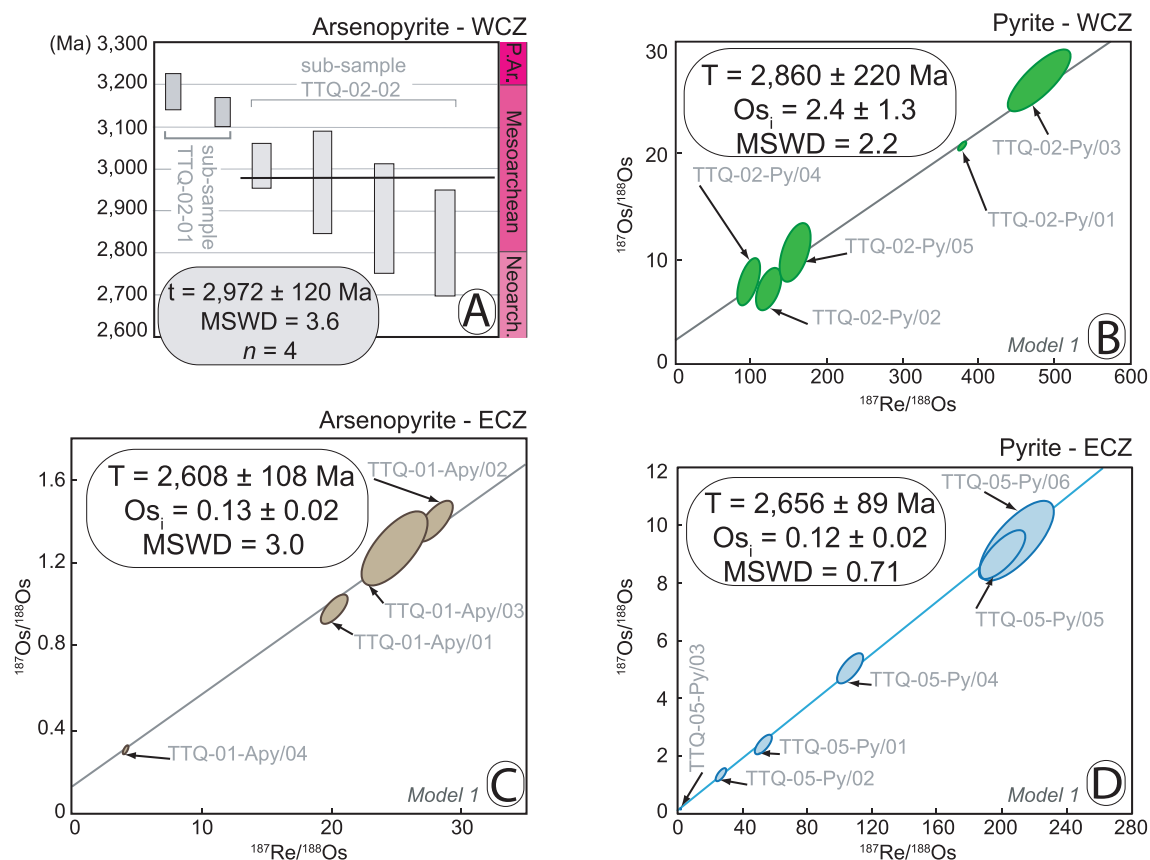
Fig. 4. Geochronological interpretation of Re-Os isotope data for arsenopyrite and pyrite at Nuuluk, Tartoq Greenstone Belt. A. Weighted average of individual Re-Os model ages constrained in the present study for arsenopyrite (n = 4, sub-sample 02, TTQ-02) in the WCZ. The individual Re-Os model ages for sub-sample 01, TTQ-02 (n = 2) yield a maximum age for massive arsenopyrite in the WCZ; B. Model 1 Re-Os isochron diagram in the $^{187}Re/^{188}Os$ vs. $^{187}Os/^{188}Os$ space for pyrite aliquots (n = 5) in the WCZ; C. Model 1 Re-Os isochron diagram in the $^{187}Re/^{188}Os$ vs. $^{187}Os/^{188}Os$ space for arsenopyrite aliquots (n = 4) in the ECZ; D. Model 1 Re-Os isochron diagram in the $^{187}Re/^{188}Os$ vs. $^{187}Os/^{188}Os$ space for pyrite aliquots (n = 6) in the ECZ. Ellipses are constructed from the maximum and minimum error vectors that are orthogonal to one another. Maximum and minimum uncertainties are statistical values that are calculated from the uncertainty of the $^{187}Os/^{188}Os$ and $^{187}Re/^{188}Os$ ratios for a given data point. Final uncertainties were calculated by full error propagation of uncertainties in the Re and Os measurements, blank values, isotopic compositions, spike calibrations, and reproducibility of the standard Re and Os values. The error correlation function, rho, is utilised for isochron regressions. The uncertainty in the ^{187}Re decay constant is included in both the isochron and model age uncertainty (after Smoliar et al. (1996) and Ludwig (2011)).

Similarly, pyrite (sample TTQ-05, $\delta^{34}S = +1.8 \pm 0.2‰$) also possesses low Re and Os concentrations: 311–585 ppt Re and 18–834 ppt total Os ($^{192}Os = 3.4–341$ ppt). Collectively, the Re-Os data of pyrite (n = 6, sample TTQ-05) yield, within uncertainty, an identical Neoarchean Re-Os isochron age of 2656 ± 89 Ma (2σ, Model 1 isochron, MSWD = 0.71, Os_i ratio = 0.12 ± 0.02; Fig. 4D).

6. Discussion

6.1. Hydrothermal alteration of oceanic crust and sub-seafloor gold-bearing arsenopyrite precursor

Arsenopyrite was the first mineral phase to precipitate in the form of massive mineralised bodies (Fig. 3). Arsenopyrite subsequently underwent minor recrystallization, brittle deformation, and finally, local dissolution and replacement by pyrite (Fig. 3). In the WCZ, arsenopyrite did not incorporate any common Os into its structure upon precipitation. As such, its present Os budget only comprises radiogenic ^{187}Os produced by the isobaric decay of ^{187}Re. The weighted average of four individual Re-Os model ages (2972 ± 120 Ma) for very coarse-grained arsenopyrite overlaps with the age range for magmatism of the Tartoq Group between < 3190 Ma and ca. 3012 Ma (Kisters et al., 2012; Szilas et al., 2013, 2014) and > 3.0 Ga prograde amphibolite-facies metamorphism (van Hinsberg et al., 2018). In addition, the Re-Os model ages of 3136 ± 33 Ma and 3184 ± 42 Ma for coarse-grained arsenopyrite (sample TTQ-02-01) are compatible with the maximum age of the Tartoq Group. This evidence indicates that the precipitation of ca. 3184–3136 Ma massive arsenopyrite is associated and coeval with the arc-related magmatism that produced the volcanic and ultramafic rocks comprising the Tartoq Group (Szilas et al., 2013, 2014). The younger ca. 2972 Ma very coarse-grained arsenopyrite (sample TTQ-02-02) may be the result of protracted hydrothermal activity leading to thickening of massive sulphide bodies, or, may be related to the coarsening of arsenopyrite through recrystallisation under the impact of > 3.0 Ga prograde amphibolite-facies metamorphism.

In light of the knowledge on the mobility of elements during hydrothermal alteration of oceanic crust, in particular in island arc magmatic systems (Falkner and Edmond, 1990; Hannington et al., 1999, 2016; Hedenquist et al., 1993; Simmons and Browne, 2000; Rae et al., 2001; Simmons and Brown, 2006, 2007; Patten et al., 2015, 2019), we propose that arsenopyrite formed as a result of hydrothermal alteration of Mesoarchean oceanic crust (Fig. 5). In addition, using the present-day Iceland setting as an analogue for the formation of Earth's earliest evolved crust (Reimink et al., 2014), we suggest that arsenopyrite could have formed massive bodies in sub-seafloor setting beneath geothermally active centres on the seafloor of the Mesoarchean ocean (cf. Polat et al., 2007). Indeed, it has been shown that hot and reduced hydrothermal fluids are able to transport Fe and As species (e.g., (As) OH_3; Heinrich and Eadington, 1986), and, lead to the precipitation of arsenopyrite in the form of seafloor to sub-seafloor semi-massive to
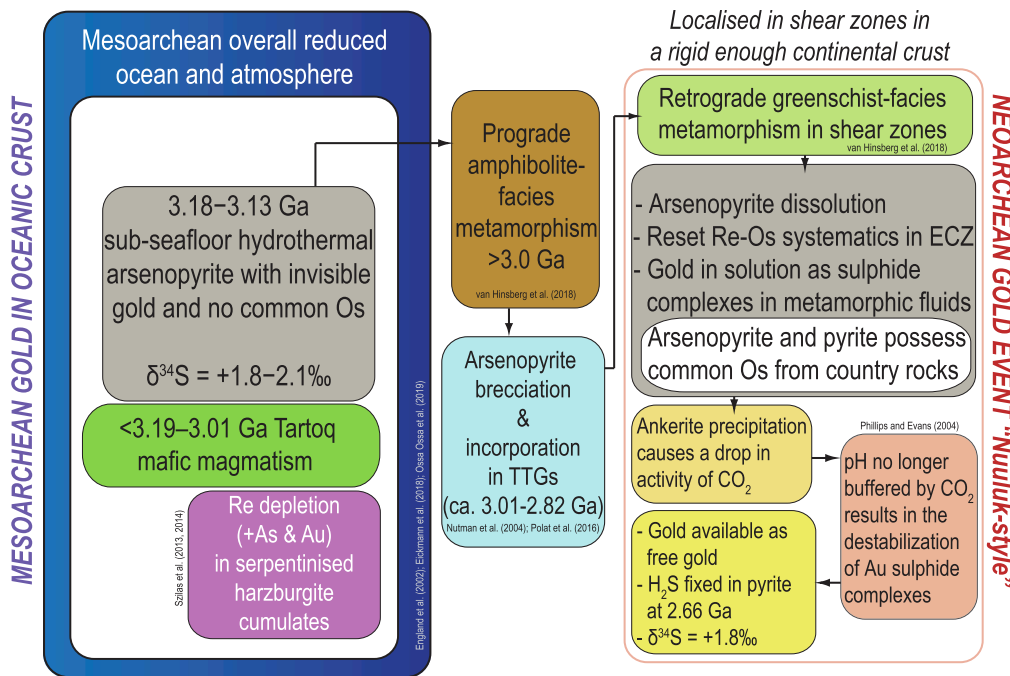
Fig. 5. Model for the gold endowment of the Mesoarchean oceanic crust and subsequent Neoarchean lode gold mineralisation in a juvenile continental crust starting from a massive arsenopyrite precursor "proto-ore", with focus on the example at Nuuluk, Tartoq greenstone belt (Petersen, 1991; Szilas et al., 2013, 2014), Greenland fragment of the North Atlantic Craton.

massive sulphides rather than stringer-type footwall mineralisation in volcanogenic massive sulphide deposits in the Phanerozoic (Heinrich and Eadington, 1986; Lydon, 1988; Hannington et al., 1999; Brueckner et al., 2015).

At Tartoq, vestiges of harzburgitic protoliths occur in the form of serpentinite. The process of serpentinisation may have caused Re and As depletion (present-day As contents of 0.6–28.0 ppm) from an ultramafic protolith that was produced by hydrous melting of the Mesoarchean mantle (Szilas et al., 2014). Arsenic, which is the most soluble chalcophile element, can be leached by hydrothermal fluids from ultramafic rocks that typically contain ca. 10–450 ppm As (Smedley and Kinniburgh, 2002; Hattori et al., 2005; Patten et al., 2015, 2019). Given the fact that As controls the accumulation of Au in Fe-sulphides and Fe-sulpharsenides (Deditius et al., 2014; Xing et al., 2019), and that As remains in solution until an As-dominant mineral phase (e.g., arsenopyrite) precipitates (Zhong et al., 2015), precipitation of hydrothermal arsenopyrite could have sequestered significant proportions of gold. Elevated Au contents in black smoker fluids and alteration profiles of present-day oceanic crust are compatible with gold being leached during hydrothermal alteration of oceanic crust (Falkner and Edmond, 1990; Hannington et al., 1999; Patten et al., 2015), and/or, more importantly, in particular in island arc magmatic systems, high gold contents are explained by magmatic volatile exsolution together with S and Se (Hedenquist et al., 1993; Simmons and Browne, 2000; Rae et al., 2001; Simmons and Brown, 2006, 2007; Hannington et al., 2016; Patten et al., 2019). In the current geodynamic setting of Iceland setting which is proposed as an analogue for the formation of Earth's earliest evolved crust (Reimink et al., 2014), sub-seafloor sulphide mineralisation may result from the boiling of chloride-bearing and neutral fluids (3.2 wt% NaCl, pH = 5–6) before discharging at black smoker seafloor vents (Hardardóttir et al., 2009, 2010; Hannington et al., 2016). Considering this analogue, we propose that such a hydrothermal sulphide mineralisation, which is highly enriched in Au and As in present-day systems (Au up to 590 ppm; Hardardóttir et al., 2009; Patten et al., 2016, 2019; Fuchs et al., 2019), could have taken the form of sub-seafloor gold-bearing arsenopyrite bodies during hydrothermal alteration of oceanic crust in the Mesoarchean.

The chemical stability of arsenopyrite in near-surface and hydrothermal environments was re-evaluated as being higher than previously thought (Pokrovski et al., 2002). Indeed, even in the presence of pyrite, arsenopyrite remains chemically stable providing that it is kept in a water-saturated and moderately reduced environment at a pH above 5. At those conditions, water in equilibrium with arsenopyrite should have dissolved arsenic concentrations in the 0.01–0.10 ppm range (Craw et al., 2003). Furthermore, the Mesoarchean shallow-marine "oxygen oases" (Eickmann et al., 2018; Ossa Ossa et al., 2019), in which reduced aqueous iron species were oxidized, would have contributed to strip the ocean from dissolved Fe^{2+} and triggered a local change from ferruginous to sulphidic waters in shallow to middle level ocean domains (Large et al., 2015). In an anoxic environment with less than 2% O_2, sulphide-driven mobilization of arsenic from arsenopyrite does not occur and arsenopyrite is not dissolved (Zhu et al., 2008). Thus, collectively taken, these thermodynamic properties and the neutral to slightly acidic pH of seawater in the Mesoarchean ocean (ca. 6.5–7.0; Shibuya et al., 2010; Halevy and Bachan, 2017; Krissansen-Totton et al., 2018) support our model and explain the stability of massive arsenopyrite bodies in sub-seafloor settings in the Mesoarchean, even in the case where a section of the oceanic crust could have been opened to "oxidizing" conditions in a shallow part of the overall reduced Mesoarchean ocean.

We suggest that the sulphur isotopic composition ($\delta^{34}S = +1.8 \pm 0.2‰$) of the ca. 2972 Ma arsenopyrite, which was preserved through medium-grade metamorphism in the Nuuluk Greenstone belt (see Section 6.2), could fit with a magmatic source of reduced sulphur. Generally, sulphur leached from igneous wall rocks or derived from magmatic fluids can account for $\delta^{34}S$ values between ca. 0 and +5‰ for sulphides in volcanic-associated deposits (Huston, 1999). Yet, the identification of the source of sulphur must discriminate between all potential pools of sulphur, including: (1) isotopic fractionation in open vs. partly open systems; (2) sulphate reduction via bacterial pathways; (3) igneous rocks and magmatic fluids. In a geothermally active Mesoarchean oceanic crust (Polat et al., 2007), hydrothermal systems in the oceanic crust could be seen as open to seawater input. Seawater in the Mesoarchean was probably mostly ferruginous with higher sulphate contents (200 μM > sulphate ≥ 5 μM) only in shallow-marine environment where a mass-dependent fractionation of ca. 20‰ between biogenic sulphides ($\delta^{34}S =$ ca. −20‰) and sulphate ($\delta^{34}S =$ ca. +3 to +8‰) could occur (Farquhar et al., 2010; Large et al., 2015; Eickmann et al., 2018). The sulphur isotopic composition of hydrothermal arsenopyrite is not

compatible with this pathway of sulphate reduction. In contrast, in agreement with the premise by Huston (1999), although not ignoring the possibility of the contribution by Mesoarchean, locally sulphidic, middle-level seawater with $\delta^{34}S$ values around 0‰ (Farquhar et al., 2007, 2010), we favour the interpretation that Mesoarchean hydrothermal systems in seafloor/sub-seafloor setting could have brought reduced sulphur derived from the Tartoq Group magmatic rocks and serpentinised harzburgite with a likely mantle-type sulphur isotopic composition traditionally considered to be 0 ± 2‰ (Thode et al., 1961; Seal, 2006), despite local sulphur heterogeneities in the early Earth mantle (Farquhar et al., 2002). Furthermore, a source of Au in the form of magmatic volatile degassing would have been accompanied by S (Patten et al., 2019) recording a magmatic sulphur isotopic signature.

In conclusion, a proto-source of Au in the Mesoarchean oceanic crust corresponds to sub-seafloor "proto-ores" made of hydrothermal arsenopyrite with primary invisible gold that formed in connection with basalt-hosted geothermal systems in an oceanic volcanic arc setting (Fig. 5). Similar systems comprising massive to semi-massive Au-Ag-Cu-rich sulphide showings have been recognized in Neoarchean greenstone belts of the Superior Province, Canada, where (1) syn-volcanic sulphides are associated with palaeo-hydrothermal alteration of basaltic lavas with pillows and breccias, and (2) massive to semi-massive arsenopyrite-pyrite are found in shear zones in those greenstone belts (Galloway et al., 2019).
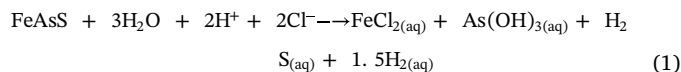
Direct evidence from petrographic observations and absolute geochronology show that this "proto-ore" is present and preserved in the WCZ where it possibly underwent subsequent yet localized tectono-metamorphic recrystallisation during prograde metamorphism. In contrast, in the ECZ, the existence of such a proto-ore is based on petrographic evidence and comparison with the WCZ to explain the resetting of the Re-Os chronometer in the massive arsenopyrite Mesoarchean "proto-ore" and incorporation of common Os derived from local surrounding rocks in the ECZ through the action of retrograde tectono-metamorphic overprint.

6.2. Prograde and retrograde metamorphism of the massive arsenopyrite precursor and gold mineralisation though secondary enrichment at 2.66 Ga

The imbrication of the Tartoq Group rocks with TTG at ca. 3012–2824 Ma is interpreted as the result of the stacking of short lived and disrupted 'slabs' of hydrated oceanic crust in an accretionary complex (Fig. 5; Nutman et al., 2004; Kisters et al., 2012; Szilas et al., 2013, 2014; Polat et al., 2016). This geodynamic setting overlapped and post-dated > 3.0 Ga prograde metamorphism of the Nuuluk part of the Tartoq greenstone belt to the amphibolite facies (~580 °C, ~4.5 kbar; van Hinsberg et al., 2018). Brittle deformation and brecciation of the competent massive arsenopyrite layers could have been coeval with or have followed this event. Yet, arsenopyrite bearing primary invisible gold remained chemically robust during amphibolite-facies metamorphism (Fougerouse et al., 2016a) and brittle deformation at Nuuluk.

Shear zones subsequently localized greenschist facies retrograde metamorphism that overprinted the peak amphibolite facies assemblage at Nuuluk (van Hinsberg et al., 2018; Fig. 5). During the retrograde metamorphism (380 ± 50 °C and < 2 kbar), small amounts of crystal plasticity of arsenopyrite is possible (e.g., with dissolution-re-precipitation of arsenopyrite), especially if the deformation vectors are at a high angle to the preferred orientation of arsenopyrite (Fougerouse et al., 2016a). In the massive arsenopyrite bodies, our petrographic observations show that pyrite precipitated where arsenopyrite was locally dissolved (Fig. 3E). This local dissolution of arsenopyrite could be a consequence of its oxidation (i.e., As^{1+} converted to As^{3+}) due to reduction of water at anodic sites on arsenopyrite crystal surfaces (Walker et al., 2006). In addition, during the strain-event arsenopyrite dissolution, the loss of gold from the crystal lattice is facilitated by localized domains of recrystallisation, most likely due to fluid

percolation along sub- and new grain boundaries (Fougerouse et al., 2016a). Therefore, in the ECZ where the gold abundances peak (20–109 ppm; Fig. 2B), the stoichiometric dissolution of a precursor arsenopyrite with primary invisible gold by small volumes of relatively low fS_2, chlorine-bearing (~0.01 M HCl) solutions may have occurred as follows (Pokrovski et al., 2002; Fougerouse et al., 2016a):

$$FeAsS + 3H_2O + 2H^+ + 2Cl^- \rightarrow FeCl_{2(aq)} + As(OH)_{3(aq)} + H_2$$

$$S_{(aq)} + 1.5H_{2(aq)} \quad (1)$$

In fact, As exists predominantly as $[As^{3+}(OH)_3]_{aq}$ (James-Smith et al., 2010; Kokh et al., 2017) in moderate temperature (> 200 °C, for this study area 380 ± 50 °C and < 2 kbar), CO_2-rich (0.05–0.25 mol %), S-bearing and low salinity (typically ≤3 wt% NaCl eq.) hydrothermal fluids responsible for "orogenic type" gold mineralisation (Mikucki, 1998; Phillips and Evans, 2004). In the ECZ, evidence for the presence of CO_2 in the fluids comes from the precipitation of ankerite in zones bearing gold mineralisation (Evans and King, 1993; Kolb, 2011; Kolb et al., 2013). The removal of CO_2 from the fluid through ankerite precipitation in the ECZ (Figs. 3A and 5) resulted in the activity of CO_2 not being high enough to continuously buffer the fluid pH. Therefore, suitable conditions for elevated gold concentration in the fluids as sulphide complexes of Au^{1+}, i.e., $AuHS^0$ and $Au(HS)^{2-}$ (Fougerouse et al., 2016; Heinrich and Eadington, 1986; Phillips and Evans, 2004; Pokrovski et al., 2002) were no longer present, and gold sulphide complexes were destabilized and gold precipitation with accompanying pyrite occurred in two principal ways: (1) at the contact between arsenopyrite and pyrite over distances of a few micrometres in the massive arsenopyrite bodies (i.e., grain boundaries; in cracks of pre-existing arsenopyrite; or within newly formed pyrite; Pokrovski et al., 2014; Xing et al., 2019), or (2) over distances of several meters within quartz-pyrite veins that were later reopened during fuchsite formation (Fig. 3G; Appel and Secher, 1984; Evans and King, 1993). At ~380 °C (tourmaline thermometry; van Hinsberg et al., 2018), it is likely that significant sulphur isotope fractionation was hampered (Seal, 2006) between the timing of dissolution of the massive arsenopyrite precursor, which is capable of preserving its sulphur isotopic composition ($\delta^{34}S = +2.1‰$) through amphibolite-facies metamorphism (cf. Wagner et al., 2004), and subsequent pyrite precipitation as indicated by the overlapping sulphur isotopic compositions of arsenopyrite ($\delta^{34}S = +2.1‰$) and pyrite ($\delta^{34}S = +1.8‰$) in the ECZ.

In the ECZ, using petrographic and isotopic evidence, we propose that the loss of gold from the crystal lattice of the arsenopyrite proto-ore through arsenopyrite dissolution under retrograde greenschist-facies conditions caused the resetting of the Re-Os isotopic system in arsenopyrite. Thus, the Re-Os isochron age of 2608 ± 108 Ma would record the best estimate for the timing of arsenopyrite dissolution. This arsenopyrite Re-Os isochron age overlaps with the pyrite Re-Os isochron age of 2656 ± 89 Ma. Considering the model of mineral precipitation presented above, the pyrite Re-Os age records the best estimate of the timing of free gold precipitation, i.e., gold that was originally present in the crystal lattice of the arsenopyrite precursor.

The significance of arsenopyrite as precursor for the formation of gold deposits is not a new concept but one that remains rather poorly explored (e.g., Fougerouse et al., 2016b). Such a process of gold upgrading/secondary enrichment through metamorphism of an arsenopyrite "proto-ore" was also conceptualized to explain the origin of the Paleoproterozoic Boliden Au-Cu-As massive sulphide deposit in Sweden (Wagner et al., 2004, 2007; Mercier-Langevin et al., 2013). The Boliden deposit records progressive recrystallization and porphyroblast growth of arsenopyrite (Wagner et al., 2007). It is proposed that invisible gold and sulphur were liberated from arsenopyrite, which underwent dissolution and replacement in response to metamorphism (Wagner et al., 2004, 2007). Both gold and sulphur were then precipitated in cross-cutting Au-rich veins in mineral phases that inherited the sulphur isotopic composition of the arsenopyrite precursor with invisible gold,

despite medium-grade metamorphism (Wagner et al., 2004, 2007). At Nuuluk, the combination of amphibolite facies prograde and greenschist facies retrograde metamorphism of Mesoarchean massive arsenopyrite precursors with invisible gold led to the secondary enrichment of gold mineralisation as free gold in lodes during the Neoarchean (Fig. 5). The same processes affected Paleoproterozoic massive arsenopyrite deposits, which were originally deposited in volcanic-arc setting, to produce younger lode gold deposits.

6.3. Insights into the palaeo-environmental conditions in arc setting in the Mesoarchean

In the WCZ, the Mesoarchean arsenopyrite proto-ore is shown to have been essentially bereft of common Os at the time of precipitation. Therefore, the overlapping and equivalent initial Os_i ratios of the Neoarchean arsenopyrite with reset Re-Os systematics ($Os_{i\text{-apy-ECZ}} = 0.13 \pm 0.02$) and the Neoarchean neo-precipitated pyrite ($Os_{i\text{-py-ECZ}} = 0.12 \pm 0.02$) in the ECZ were not derived from Os present in a massive arsenopyrite precursor of presumed Mesoarchean age in the ECZ. Instead, it is most likely that arsenopyrite and pyrite acquired their initial Os isotopic composition from the surrounding serpentinised Mesoarchean harzburgite protoliths and volcanic rocks of the Tartoq Group. For these Mesoarchean Tartoq Group rocks, we suggest an original Os isotopic composition of 0.11 ± 0.01 that is equivalent to the hypothetical primitive Mesoarchean upper mantle (Os_M) at 3200–2800 Ma, calculated by using the present-day values of $^{187}Re/^{188}Os = 0.435 \pm 0.055$ and $^{187}Os/^{188}Os = 0.130 \pm 0.001$ for a primitive upper mantle (Meisel et al., 2001; Carlson, 2005). The Os_i ratios of Neoarchean arsenopyrite and pyrite, which overlap with the Os_M isotopic composition of the Mesoarchean mantle, preclude any addition of radiogenic Os that would have elevated the Os_i ratios of Neoarchean arsenopyrite and pyrite to values significantly higher than 0.11 at the time of mineral precipitation. Therefore, we dismiss a regional contribution in Os by crustal fluids released from evolved crustal lithologies (i.e., with high Re/Os ratios and significant accumulation of ^{187}Os through decay of ^{187}Re) involved in the accretionary complex. Instead, in the ECZ, Os is interpreted to have been only derived locally. In addition, the Os_i initial ratio of pyrite in the WCZ, for which petrographic evidence show that it post-dates and replaces arsenopyrite, seems to confirm this local derivation of Os by metamorphic fluids. Indeed, although imprecise, the Re-Os isochron age for pyrite in the WCZ possesses an Os_i ratio of 2.4 ± 1.3 (i.e, $Os_i > 1.1$). This Os_i ratio for pyrite in the WCZ is significantly higher than the estimate for the primitive Mesoarchean mantle.

In the arc setting proposed for deposition of the Tartoq Group, near-shore, shallow marine environments might have been slightly oxygenated in spite of the clear presence of an overall reduced Mesoarchean atmosphere (England et al., 2002; Eickmann et al., 2018; Ossa Ossa et al., 2018, 2019). Osmium readily dissolves, in particular under high Eh and acidic pH conditions (Wimpenny et al., 2007). Therefore, weathering conditions, which exert a significant influence on Os behaviour in the surface to sub-surface environment (Wimpenny et al., 2007), might have been oxidising enough in near-shore, shallow marine setting with slightly acidic to neutral seawater in the Mesoarchean (Shibuya et al., 2010; Szilas and Garde, 2013; Halevy and Bachan, 2017; Krissansen-Totton et al., 2018). Under these conditions, Os would have been mobilised from the surrounding lithologies in the Tartoq Group (e.g., Os-rich ultramafic rocks) into the shallow-marine water column. Extensive graphite-bearing schists in the WCZ (Fig. 2B), which are closely associated with the Tartoq Group serpentinites and volcanic rocks, might represent former carbonaceous sedimentary horizons (Kolb et al., 2013; Large et al., 2015), which are known as sinks possibly enriched in Re and Os in the geological record (e.g., Ravizza and Turekian, 1989; Cohen et al., 1999; Selby and Creaser, 2003). Thus, those carbonaceous sediments could have been deposited and scavenged Re and Os from a shallow-marine water column. With

subsequent radiogenic decay of ^{187}Re in carbonaceous sediments and subsequent metamorphism, radiogenic Os could have been contributed by metamorphic fluids to pyrite in the WCZ.

7. Conclusion

The strength of our work lies in the geologically robust, high-quality Re-Os ages for arsenopyrite and pyrite. These new data, combined with our detailed petrographic observations and existing age data for the wider study area, support the conclusion that hydrothermal arsenopyrite related to arc volcanism formed in sub-seafloor setting in the Mesoarchean (arsenopyrite Re-Os model age), prior to acting as the principal source for lode gold in younger Neoarchean (pyrite Re-Os isochron age) orogenic-type deposits in the area.

In the present study, a model for a peculiar and non-negligible proto-source of gold in the Mesoarchean oceanic crust is emerging: (1) primary extraction of Au from the Mesoarchean mantle at the time of ca. < 3.19–3.01 Ga basalt magmatism and associated lower crustal harzburgite cumulates; (2) As, Re, and Au contributed by magmatic volatile exsolution and alteration of the upper oceanic crust through hydrothermal cell circulation and serpentinisation of the lower crustal harzburgite cumulates; (3) hydrothermal systems precipitating sub-seafloor massive arsenopyrite bodies with invisible gold at ca. 3.18–3.13 Ga, (4) arsenopyrite retaining gold and remaining chemically robust during > 3.0 Ga prograde amphibolite-facies metamorphism path and during imbrication of the Tartoq greenstone belt and TTGs at ca. 3.01–2.82 Ga; (5) retrograde greenschist-facies metamorphic overprint localized in shear zones at Nuuluk when the crystal plasticity of arsenopyrite caused its local dissolution, the resetting of its Re-Os geochronometer with a Neoarchean age in areas of major gold loss (in particular in the ECZ); (6) secondary enrichment of primary invisible gold in Mesoarchean massive arsenopyrite through retrograde metamorphism focused within shear zones into lodes in the juvenile continental crust that contain free gold associated with newly formed ca. 2.66 Ga pyrite.

A peak in lode gold or orogenic-type gold deposits occurred between ca. 2.75 and 2.55 Ga during a "Neoarchean Global Gold Event" (Goldfarb et al., 2001, 2005; Bierlein et al., 2006), which coincides with the time when the juvenile continental crust had become able to sustain plate tectonics and record strong regional deformation fabrics. Thus, in light of the two mineralising events identified in the Tartoq greenstone belt in the Greenland fragment of the North Atlantic Craton, we contribute a more general working hypothesis suggesting a connection between a ca. 3.18–3.13 Ga gold proto-source in sub-seafloor arsenopyrite in arc-related Mesoarchean greenstone belts, and, the ca. 2.75–2.65 Ga "Global Gold Event" representing the gold endowment of the juvenile continental crust in stabilising cratons through metamorphic upgrading of the Mesoarchean proto-source.

Competing interests

Within the last three years, both Joshua W. Hughes and Denis M. Schlatter have provided consultancy to AEX Gold Inc., the current exploration licence holder of the Tartoq greenstone belt. However, their involvement concerns the company's other exploration properties and has not incorporated the Tartoq greenstone belt. The other authors declare no competing interest.

Author contributions

NJS, DS, and JWH designed the study based on samples and detailed geological background provided by JWH. NJS carried out all petrographic investigations followed by sample preparation, quality control of the mineral separates and, Re-Os isotope geochemistry and mass spectrometry analyses. DMS and JK provided extensive knowledge of the metallogeny and geodynamic evolution of the Greenland fragment of the North Atlantic Craton. AB carried out sulphur isotope analyses of the aliquots provided by NJS. NJS wrote the manuscript and all other authors contributed comments and edits to the manuscript.

Data and material availability

All data are available in the present publication. Correspondence and material requests should be addressed to corresponding author N.J. Saintilan.

References

Anhaeusser, C.R., Fritze, K., Fyfe, W.S., Gill, R.C.O., 1975. Gold in "primitive" Archaean volcanics. Chem. Geol. 16, 129–135.

Appel, P.W.U., Secher, K., 1984. On a gold mineralisation in the Precambrian Tartoq Group, SW Greenland. J. Geol. Soc. 141, 273–278.

Barboni, M., Boehnke, P., Keller, B., Kohl, I.E., Schoene, B., Young, E.D., McKeegan, K.D., 2017. Early formation of the Moon 4.51 billion years ago. Sci. Adv. 3, e1602365.

Bierlein, F.P., Groves, D.I., Goldfarb, R.J., Dubé, B., 2006. Lithospheric controls on the formation of provinces hosting giant orogenic gold deposits. Mineral Deposita 40, 874–886.

Bodiselitsch, B., Koeberl, C., Master, S., Reimold, W.U., 2005. Estimating duration and intensity of Neoproterozoic Snowball glaciations from Ir anomalies. Science 308, 239–242.

Brenan, J.M., McDonough, W.F., 2009. Core formation and metal-silicate fractionation of osmium and iridium from gold. Nat. Geosci. 2, 798–801.

Brueckner, S.M., Piercey, S.J., Layne, G.D., Piercey, G., Sylvester, P.J., 2015. Variations of sulphur isotope signatures in sulphides from the metamorphosed Ming Cu(-Au) volcanogenic massive sulphide deposit, Newfoundland Appalachians. Canada. Miner. Deposita 50, 619–640.

Brügmann, G.E., Arndt, N.T., Hofmann, A.W., Tobschall, H.J., 1987. Noble metal abundance in komatiite suites from Alexo, Ontario, and Gorgona Island, Colombia. Geochim. Cosmochim. Acta 51, 2159–2169.

Carlson, R.W., 2005. Application of the Pt-Re-Os isotopic systems to mantle geochemistry and geochronology. Lithos 82, 249–272.

Cohen, A.S., Coe, A.L., Bartlett, J.M., Hawkesworth, C.J., 1999. Precise Re-Os ages of organic-rich mudrocks and the Os isotopic composition of Jurassic seawater. Earth Planet. Sci. Lett. 167, 159–173.

Craw, D., Falconer, D., Youngson, J.H., 2003. Environmental arsenopyrite stability and dissolution: theory, experiment, and field observations. Chem. Geol. 199, 71–82.

Creaser, R.A., Papanastassiou, D.A., Wasserburg, G.J., 1991. Negative thermal ion mass spectrometry of osmium, rhenium and iridium. Geochim. Cosmochim. Acta 55, 191–213.

Deditius, A.P., Reich, M., Kesler, S.E., Utsunomiya, S., Chryssoulis, S.L., Walshe, J., Ewing, R.C., 2014. The coupled geochemistry of Au and As in pyrite from hydrothermal ore deposits. Geochim. Cosmochim. Acta 140, 644–670.

Dziggel, A., Diener, J.F.A., Kolb, J., Kokfelt, T., 2014. Metamorphic record of accretionary processes during the Neoarchaean: the Nuuk region, southern West Greenland. Precambr. Res. 242, 22–38.

Dziggel, A., Kokfelt, T.F., Kolb, J., Kisters, A.F.M., Reifenröther, R., 2017. Tectonic switches and the exhumation of deep-crustal granulites during Neoarchean terrane accretion in the area around Grædefjord, SW Greenland. Precambr. Res. 300, 223–245.

Eickmann, B., Hofmann, A., Wille, M., Bui, T.H., Wing, B.A., Schoenberg, R., 2018. Isotopic evidence for oxygenated Mesoarchaean shallow oceans. Nat. Geosci. 11, 133–138.

England, G.L., Rasmussen, B., Krapez, B., Groves, D.I., 2002. Paleoenvironmental significance of rounded pyrite in siliciclastic sequences of the Late Archaean Witwatersrand Basin: oxygen-deficient atmosphere or hydrothermal alteration? Sedimentology 49, 1133–1156.

Evans, D.M., King, A.R., 1993. Sediment and shear-hosted gold mineralisation of the Tartoq Group supracrustals, southwest Greenland. Precambr. Res. 62, 61–66.

Falkner, K.K., Edmond, J.M., 1990. Gold in seawater. Earth Planet. Sci. Lett. 98, 208–221.

Farquhar, J., Wing, B.A., McKeegan, K.D., Harris, J.W., Cartigny, P., Thiemens, M.H., 2002. Mass-independent sulfur of inclusions in diamond and sulfur recycling on Early Earth. Science 298, 2369–2372.

Farquhar, J., Peters, M., Johnston, D.T., Strauss, H., Masterson, A., Wiechert, U., Kaufman, A.J., 2007. Isotopic evidence for Mesoarchean anoxia and changing atmospheric sulphur chemistry. Nature 449, 706–709.

Farquhar, J., Wu, N., Canfield, D.E., Oduro, H., 2010. Connections between sulfur cycle evolution, sulfur isotopes, sediments, and base metal sulphide deposits. Econ. Geol. 105, 509–533.

Fougerouse, D., Micklethwaite, S., Halfpenny, A., Reddy, S.M., Cliff, J.B., Martin, L.A.J., Kilburn, M., Guagliardo, P., Ulrich, S., 2016a. The golden ark: arsenopyrite crystal plasticity and the retention of gold through high strain and metamorphism. Terra Nova 28, 181–187.

Fougerouse, D., Reddy, S.M., Saxey, D.W., Rickard, W.D.A., van Riessen, A., Micklethwaite, S., 2016b. Nanoscale gold clusters in arsenopyrite controlled by growth crate not concentration: evidence from atom probe microscopy. Am. Mineral. 101, 1916–1919.

Friend, C.R.L., Nutman, A.P., McGregor, V.R., 1988. Late Archaean terrane accretion in the Godthåb region, southern West Greenland. Nature 335, 535–538.

Friend, C.R.L., Nutman, A.P., Baadsgaard, H., Kinny, P.D., McGregor, V.R., 1996. Timing of late Archaean terrane assembly, crustal thickening and granite emplacement in the Nuuk region, southern West Greenland. Earth Planet. Sci. Lett. 142, 353–365.

Frimmel, H.E., 2014. A giant Mesoarchaean crustal gold-enrichment episode: possible causes and consequences for exploration. In: Kelley, K., Golden, H.C. (Eds.), Building Exploration Capability for the 21st Century. Society of Economic Geologists, Special Publication 18, pp. 209–234.

Frimmel, H.E., 2018. Episodic concentration of gold to ore grade through Earth's history. Earth Sci. Rev. 180, 148–158.

Frimmel, H.E., 2019. The Witwatersrand Basin and its gold deposits. In: Kröner, A., Hofmann, A. (Eds.), The Archaean Geology of the Kaapvaal Craton, Southern Africa. Regional Geology Reviews. Springer, pp. 255–275.

Fuchs, S., Hannington, M.D., Petersen, 2019. Divining gold in seafloor polymetallic massive sulfide systems. Mineral. Deposita 54, 789–820.

Galloway, S., Ross, P.-S., Bandyayera, D., Daoudene, Y., 2019. Contemporaneously erupted tholeiitic and calc-alkaline magmas in the Archaean Colomb-Chaboullié greenstone belt, James Bay, Quebec: petrologic implications. Precambr. Res. 331, 105363.

Glikson, A.Y., 2001. The astronomical connection of terrestrial evolution: crustal effects of post-3.8 Ga mega-impact clusters and evidence for major 3.2 ± 0.1 Ga bombardment of the Earth-Moon system. J. Geodyn. 32, 205–229.

Glikson, A.Y., Vickers, J., 2006. The 3.26–3.24 Ga Barberton asteroid impact cluster: tests of tectonic and magmatic consequences, Pilbara Craton, Western Australia. Earth. Planet. Sci. Lett. 241, 11–20.

Goldfarb, R.J., Groves, D.J., Gardoll, S., 2001. Orogenic gold and geologic time: a global synthesis. Ore Geol. Rev. 18, 1–75.

Goldfarb, R., Baker, T., Dube, B., Groves, D.I., Hart, C.J., Gosselin, P., 2005. Distribution, character and genesis of gold deposits in metamorphic terranes. Soc. Econ. Geol. 407–450.

Goldfarb, R.J., Bradley, D., Leach, D.L., 2010. Secular variation in economic geology. Econ. Geol. 105, 459–465.

Greber, N.D., Dauphas, N., Bekker, A., Ptáček, M.P., Bindeman, I.N., Hofmann, A., 2017. Titanium isotopic evidence for felsic crust and plate tectonics 3.5 billion years ago. Science 357, 1271–1274.

Groves, D.I., Condie, K.C., Goldfarb, R.J., Hronsky, J.M.A., Vielreicher, R.M., 2005. Secular changes in global tectonic processes and their influence on the temporal distribution of gold-bearing mineral deposits. Econ. Geol. 100, 203–224.

Halevy, I., Bachan, A., 2017. The geologic history of seawater pH. Science 355, 1069–1071.

Hannington, M.D., Poulsen, K.H., Thompson, J.F.H., Sillitoe, R.H., 1999. Chapter 14. Volcanogenic gold in the massive sulphide environment. In: Barrie, C.T., Hannington, M.D. (Eds.), Volcanic-Associated Massive Sulphide Deposits: Processes and Examples in Modern and Ancient Settings, vol. 8 Rev. in Econ. Geol. Society of Economic Geologists, Boulder, CO, pp. 319–350.

Hannington, M.D., Harðardóttir, V., Garde-Schönberg, D., Brown, K.L., 2016. Gold enrichment in active geothermal systems by accumulating colloidal suspensions. Nat. Geosci. 9, 1–5.

Hao, J., Sverjensky, D.A., Hazen, R.M., 2019. Redox states of Archean surficial environments: the importance of H_2, g instead of O_2, g for weathering reactions. Chem. Geol. 521, 49–58.

Hardardóttir, V., Brown, K.L., Fridriksson, T., Hedenquist, J.W., Hannington, M.D., Thorhallsson, S., 2009. Metals in deep liquid of the Reykjanes geothermal system, southwest Iceland: implications for the composition of seafloor black smoker fluids. Geology 37, 1103–1106.

Hardardóttir, V., Hannington, M., Hedenquist, J., Kjarsgaard, I., Hoal, K., 2010. Cu-rich scales in the Reykjanes geothermal system, Iceland. Econ. Geol. 105, 1143–1155.

Hastie, A.R., Fitton, J.G., Bromley, G.D., Butler, I.B., Odling, N.W.A., 2016. The origin of Earth's first continents and the onset of plate tectonics. Geology 44, 855–858.

Hattori, K., Takahashi, Y., Guillot, S., Johanson, B., 2005. Occurrence of arsenic (V) in forearc mantle serpentinites based on X-ray absorption spectroscopy study. Geochim. Cosmochim. Acta 69, 5585–5596.

Hawkesworth, C.J., Cawood, P.A., Dhuime, B., 2019. Rates of generation and growth of the continental crust. Geosci. Front. 10, 165–173.

Hedenquist, J.W., Simmons, S.F., Giggenbach, W.F., Eldridge, C.S., 1993. White Island, New Zealand, volcanic-hydrothermal system represented the geochemical environment of high-sulfidation Cu and Au ore deposition. Geology 21, 731–734.

Heinrich, C.A., 2015. Witwatersrand gold deposits formed by volcanic rain, anoxic rivers and Archaean life. Nat. Geosci. 8, 206–209.

Heinrich, C.A., Eadington, P.J., 1986. Thermodynamic predictions of the hydrothermal chemistry of arsenic and their significance for the paragenetic sequence of some cassiterite-arsenopyrite-base metal sulfide deposits. Econ. Geol. 81, 511–529.

Hofmann, A., Pitcairn, I., Wilson, A., 2017. Gold mobility during Palaeoarchaean submarine alteration. Earth Planet. Sci. Lett. 462, 47–54.

Huston, D.L., 1999. Stable isotopes and their significance for understanding the genesis of volcanic-hosted massive sulphide deposits: a review. In: Barrie, C.T., Hannington, M.D. (Eds.), Volcanic-associated Massive Sulphide Deposits: Processes and Examples in Modern and Ancient Settings, vol. 8 Rev. in Econ. Geol. Society of Economic Geologists, Boulder, CO, pp. 157–179.

James-Smith, J., Cauzid, J., Testemale, D., Liu, W., Hazemann, J.-L., Proux, O., Etschmann, B., Philippot, P., Banks, D., Williams, P., Brügger, J., 2010. Arsenic speciation in fluid inclusions using micro-beam X-ray absorption spectroscopy. Am. Mineral. 95, 921–932.

Johnson, T.E., Kirkland, C.L., Gardiner, N.J., Brown, M., Smithies, R.H., Santosh, M., 2019. Secular change in TTG compositions: implications for the evolution of Archaean geodynamics. Earth Planet. Sci. Lett. 505, 65–75.

King, A.R., 1985. Greenex A/S Sermiligaarsuk Exploration Concession. Report on geological field Work Carried Out in the Sermiligaarsuk Fjord Area, South-west Greenland, July-August (Greenex A/S).

Krissansen-Totton, J., Arney, G.N., Catling, D.C., 2018. Constraining the climate and ocean pH of the early Earth with a geological carbon cycle model. Proc. Natl. Acad. Sci. 115, 4105–4110.

Kisters, A.F.M., van Hinsberg, V.J., Szilas, K., 2012. Geology of an Archaean accretionary complex – the structural record of burial and return flow in the Tartoq Group of South West Greenland. Precambr. Res. 220–221, 107–122.

Koglin, N., Zeh, A., Frimmel, H.E., Gerdes, A., 2010. New constraints on the auriferous Witwatersrand sediment provenance from combined detrital zircon U-Pb and Lu-Hf isotope data for the Eldorado Reef (Central Rand Group, South Africa). Precambr. Res. 183, 817–824.

Kokh, M.A., Akinfiev, N.N., Pokrovski, G.S., Salvi, S., Guillaume, D., 2017. The role of carbon dioxide in the transport and fractionation of metals by geological fluids. Geochim. Cosmochim. Acta 197, 433–466.

Kolb, J., 2011. Controls of Hydrothermal Quartz Vein Mineralisation and Wall Rock Alteration in the Paamiut and Tartoq Areas, South-West Greenland, 2011/114. Geological Survey of Denmark and Greenland, Copenhagen.

Kolb, J., Kokfelt, T., Dziggel, A., 2012. Deformation history of an Archaean terrane at mid-crustal level: the Tasiusarsuaq terrane of southern West Greenland. Precambr. Res. 212–213, 34–56.

Kolb, J., Dziggel, A., Schlatter, D.M., 2013. Gold occurrences of the Archaean North Atlantic craton, southwestern Greenland: a comprehensive genetic model. Ore Geol. Rev. 54, 29–58.

Large, R.R., Gregory, D.D., Steadman, J.A., Tomkins, A.G., Lounejeva, E., Danyushevsky, L.V., Halpin, J.A., Maslennikov, V., Sack, P.J., Mukherjee, I., Berry, R., Hickman, A., 2015. Gold in the oceans through time. Earth Planet. Sci. Lett. 428, 139–150.

Laurent, O., Björnsen, J., Wotzlaw, J.-F., Bretscher, S., Pimenta Silva, M., Moyen, J.-F., Ulmer, P., Bachmann, O., 2020. Earth's earliest granitoids are crystal-rich magma reservoirs tapped by silicic eruptions. Nat. Geosci. https://doi.org/10.1038/s41561-019-0520-6.

Lowe, D.R., Byerly, G.R., 2018. The terrestrial record of the Late Heavy Bombardment. New Astro. Rev. 81, 39–61.

Ludwig, K., 2011. Isoplot, Version 4.15: A Geochronological Toolkit for Microsoft Excel. Berkley Geochronology Centre Special Publication 4.

Lydon, J.W., 1988. Volcanogenic massive sulphide deposits. Part 2: genetic models. Geosci. Can. 15, 43–65.

Meisel, T., Walker, R.J., Irving, A.J., Lorand, J.-P., 2001. Osmium isotopic compositions of mantle xenoliths. Geochim. Cosmochim. Acta 65, 1311–1323.

Mercier-Langevin, P., McNicoll, V., Allen, R., Blight, J.H.S., Dubé, B., 2013. The Boliden gold-rich volcanogenic massive sulphide deposit, Skellefte district, Sweden: new U-Pb age constraints and implications at deposit and district scale. Mineral. Deposita 48, 485–504.

Mikucki, E.J., 1998. Hydrothermal transport and depositional processes in Archaean lode-gold systems: a review. Ore Geol. Rev. 13, 307–321.

Næraa, T., Scherstén, A., Rosing, M.T., Kemp, A.I.S., Hoffmann, J.E., Kokfelt, T.F., Whitehouse, M.J., 2012. Hafnium isotope evidence for a transition in the dynamics of

continental growth 3.2 Gyr ago. Nature 485, 627–631.

Nagel, T.J., Hoffmann, J.E., Münker, C., 2012. Generation of Eoarchean tonalite-trondhjemite-granodiorite series from thickened mafic crust. Geology 40, 375–378.

Nielsen, B.L., 1976. Economic minerals. In: Escher, A., Watt, W.S. (Eds.), Geology of Greenland. The Geological Survey of Greenland, Copenhagen, pp. 460–487.

Nutman, A.P., Friend, C.R.L., 2007. Adjacent terranes with ca. 2715 and 2650 Ma high-pressure metamorphic assemblages in the Nuuk region of the North Atlantic Craton, southern West Greenland: complexities of Neoarchaean collisional orogeny. Precambr. Res. 155, 159–203.

Nutman, A.P., Friend, C.R.L., Baadsgaard, H., McGregor, V.R., 1989. Evolution and assembly of Archaean gneiss terranes in the Godthåbsfjord region, southern West Greenland: structural, metamorphic, and isotopic evidence. Tectonics 8, 573–589.

Nutman, A.P., Friend, C.R.L., Barker, S.S., McGregor, V.R., 2004. Inventory and assessment of Paleoarchaean gneiss terrains and detrital zircons in southern west Greenland. Precambr. Res. 135, 281–314.

O'Neil, J., Carlson, R.W., 2017. Building Archaean cratons from Hadean mafic crust. Science 355, 1199–1202.

O'Neil, J., Carlson, R.W., Papineau, D., Levine, E.Y., Francis, D., 2019. The Nuvvuagittuq Greenstone Belt: a glimpse of Earth's earliest crust. In: van Kranendonk, M.J., Bennett, V.C., Hoffman, J.E. (Eds.), Earth's Oldest Rocks, second ed. Elsevier, Amsterdam, the Netherlands, pp. 349–372.

Ossa Ossa, F., Hofmann, A., Wille, M., Spangenberg, J.E., Bekker, A., Poulton, S.W., Eickmann, B., Schoenberg, R., 2018. Aerobic iron and manganese cycling in a redox-stratified Mesoarchean epicontinental sea. Earth Planet. Sci. Lett. 500, 28–40.

Ossa Ossa, F., Hofmann, A., Spangenberg, J.E., Poulton, S.W., Stüeken, E.E., Schœnberg, R., Eickmann, B., Wille, M., Butler, M., Bekker, A., 2019. Limited oxygen production in the Mesoarchaean ocean. Proc. Natl. Acad. Sci. U.S.A. https://doi.org/10.1073/pnas.1818762116.

Patten, C.G., Pitcairn, I.K., Teagle, D.A., Harris, M., 2015. Mobility of Au and related elements during the hydrothermal alteration of oceanic crust: implications for the sources of metals in VMS deposits. Mineral. Deposita 51, 179–200.

Patten, C.G.C., Pitcairn, I.K., Teagle, D.A.H., Harris, M., 2016. Sulphide mineral evolution and metal mobility during alteration of the oceanic crust; Insights from ODP Hole 1256D. Geochim. Cosmochim. Acta 193, 132–159.

Patten, C.G.C., Pitcairn, I.K., Alt, J.C., Zack, T., Lahaye, Y., Teagle, D.A.H., Markdahl, K., 2019. Metal fluxes during magmatic degassing in the oceanic crust: sulfide mineralisation at ODP site 768B, Izu-Bonin forearc. Mineral. Deposita. https://doi.org/10.1007/s00126-019-00900-9.

Petersen, J.S., 1991. Nuuluk-Iterlak gold and massive-sulfide project, Tartoq Archaean greenstone belt, SW Greenland: Field Report. Nunaoil A/S.

Phillips, G.N., Evans, K.A., 2004. Role of CO_2 in the formation of gold deposits. Nature 429, 860–863.

Pokrovski, G.S., Kara, S., Roux, J., 2002. Stability and solubility of arsenopyrite, FeAsS, in crustal fluids. Geochim. Cosmochim. Acta 66, 2361–2378.

Pokrovski, G.S., Akinfiev, N.N., Borisova, A.Y., Zotov, A.V., Kouzmanov, K., 2014. Gold speciation and transport in geological fluids: insights from experiments and physical-chemical modelling. Geol. Soc. London Spec. Publ. 402, 9–70.

Polat, A., Appel, P.W.U., Frei, R., Pan, Y., Dilek, Y., Ordóñez-Calderón, J.C., Fryer, B., Hollis, J.A., Raith, J.G., 2007. Field and geochemical characteristics of the Mesoarchean (~3075 Ma) Ivisaartoq greenstone belt, southern West Greenland: evidence for seafloor hydrothermal alteration in supra-subduction oceanic crust. Gond. Res. 11, 69–91.

Polat, A., Kokfelt, T., Burke, K.C., Kusky, T.M., Bradley, D.C., Dziggel, A., Kolb, J., 2016. Lithological, structural and geochemical characteristics of the Mesoarchaean Tartoq Greenstone Belt, Southern West Greenland, and the Chugach – Prince William Accretionary Complex, Southern Alaska: evidence for uniformitarian plate-tectonic processes. Can. J. Earth Sci. 53, 1336–1371.

Rae, A.J., Cooke, D.R., Brown, K.L., 2001. The trace metal chemistry of deep geothermal water, Palinpinon Geothermal Field, Negros Island, Philippines: implications for precious metal deposition in epithermal gold deposits. Econ. Geol. 106, 1425–1426.

Ravizza, G., Turekian, K.K., 1989. Application of the ^{187}Re-^{187}Os system to black shale geochronometry. Geochim. Cosmochim. Acta 53, 3257–3262.

Reimink, J.R., Chacko, T., Stern, R.A., Heaman, L.M., 2014. Earth's earliest evolved crust generated in an Iceland-like setting. Nat. Geosci. 7, 529–533.

Reimink, J.R., Davies, J.H.F.L., Chacko, T., Stern, R.A., Heaman, L., Sarkar, C., Schaltegger, U., Creaser, R.A., Pearson, D.G., 2016. No evidence for Hadean continental crust within Earth's oldest evolved rock unit. Nat. Geosci. 9, 777–780.

Robinson, B.W., Kusakabe, M., 1975. Quantitative preparation of sulfur dioxide for 34S/32S analyses from sulfides by combustion with cuprous oxide. Anal. Chem. 47, 1179–1181.

Russill, J, Kellaway, B, 2017. Exploring Greenland's gold districts. SRK News(57).

Scherstén, A., Szilas, K., Creaser, R.A., Næraa, T., van Gool, J.A.M., Østergaard, C., 2012. Re-Os and U-Pb constraints on gold mineralisation events in the Meso- to Neoarchaean Storø greenstone belt, Storø, Greenland. Precambr. Res. 200–203, 149–162.

Seal, R.R., 2006. Sulfur isotope geochemistry of sulphide minerals. Rev. Mineral. Geochem. 61 (1), 633–677.

Selby, D., Creaser, R.A., 2003. Re-Os geochronology of organic-rich sediments: an evaluation of organic matter analysis methods. Chem. Geol. 200, 225–240.

Selby, D., Kelley, K.D., Hitzman, M., Zieg, J., 2009. Re-Os sulfide (bornite, chalcopyrite, and pyrite) systematics of the carbonate-hosted copper deposits at Ruby Creek, Southern Brooks Range, Alaska. Econ. Geol. 104, 437–444.

Shahar, A., Driscoll, P., Weinberger, A., Cody, G., 2019. What makes a planet habitable? Science 364, 434–435.

Shibuya, T., Komiya, T., Nakamura, K., Takai, K., Maruyama, S., 2010. Highly alkaline, high-temperature hydrothermal fluids in the early Archean ocean. Precambr. Res.

182, 230–238.

Shirey, S.B., Walker, R.J., 1995. Carius tube digestion for low-blank rhenium-osmium analysis. Anal. Chem. 67, 2136–2141.

Shirey, S.B., Richardson, S.H., 2011. Start of the Wilson cycle at 3 Ga shown by diamonds from subcontinental mantle. Science 333, 434–436.

Simmons, S.F., Browne, P.R.L., 2000. Hydrothermal minerals and precious metals in the Broadlands-Ohaaki geothermal system: implications for understanding low-sulfidation epithermal environments. Econ. Geol. 95, 971–999.

Simmons, S.F., Brown, K.L., 2006. Gold in magmatic hydrothermal solutions and the rapid formation of a giant ore deposit. Science 314, 288–291.

Simmons, S.F., Brown, K.L., 2007. The flux of gold and related metals through a volcanic arc, Taupo Volcanic Zone, New Zealand. Geology 35, 1009–1102.

Smedley, P.L., Kinniburgh, D.G., 2002. A review of the source, behavior and distribution of arsenic in natural waters. Appl. Geochem. 17, 517–568.

Smit, K.V., Shirey, S.B., Hauri, E.H., Stern, R.A., 2019. Sulfur isotopes in diamonds reveal differences in continent construction. Science 364, 383–385.

Smoliar, M.I., Walker, R.J., Morgan, J.W., 1996. Re-Os isotope constraints on the age of Group IIA, IIIA, and IVB iron meteorites. Science 271, 1099–1102.

Steenfelt, A., Kolb, J., Thrane, K., 2016. Metallogeny of South Greenland: a review of geological evolution, mineral occurrences and geochemical exploration data. Ore Geol. Rev. 77, 194–245.

Szilas, K., Garde, A.A., 2013. Mesoarchean aluminous rocks at Storø, southern West Greenland: new age data and evidence of premetamorphic seafloor weathering of basalts. Chem. Geol. 354, 124–138.

Szilas, K., van Hinsberg, V.J., Kisters, A.F., Hoffmann, J.E., Kokfelt, T.F., Scherstén, A., Windley, B.F., Münker, C., 2013. Remnants of arc-related Mesoarchaean oceanic crust in the Tartoq Group, SW Greenland. Gond. Res. 23, 436–451.

Szilas, K., van Hinsberg, V.J., Creaser, R.A., Kisters, A.F., 2014. The geochemical composition of serpentinites in the Mesoarchaean Tartoq Group, SW Greenland: Harzburgitic cumulates or melt-modified mantle? Lithos 198–199, 103–116.

Tang, M., Chen, K., Rudnick, R.L., 2016. Archaean upper crust transition from mafic to felsic marks the onset of plate tectonics. Science 351, 372–375.

Thode, H.G., Monster, J., Dunford, H.B., 1961. Sulfur isotope geochemistry. Geochim. Cosmochim. Acta 25, 159–174.

van Hinsberg, V.J., Crotty, C., Roozen, S., Szilas, K., Kisters, A.F., 2018. Pressure-temperature history of the > 3 Ga Tartoq greenstone belt in Southwest Greenland and its implication for Archaean tectonics. Geoscience 8, 367.

Völkening, J., Walczyk, T., Heumann, K., 1991. Osmium isotopic ratio determination by negative thermal ionization mass spectrometry. Int. J. Spectro. Ionic Phys. 105, 147–159.

Wagner, T., Boyce, A.J., Jonsson, E., Fallick, A.E., 2004. Laser microprobe sulphur isotope analysis of arsenopyrite: experimental calibration and application to the Boliden Au-Cu-As massive sulphide deposit. Ore Geol. Rev. 25, 311–325.

Wagner, T., Klemd, R., Wenzel, T., Mattsson, B., 2007. Gold upgrading in metamorphosed massive sulfide ore deposits: direct evidence from laser-ablation-inductively coupled plasma-mass spectrometry analysis of invisible gold. Geology 35, 775–778.

Walker, F.P., Schreiber, M.E., Rimstidt, J.D., 2006. Kinetics of arsenopyrite oxidative dissolution by oxygen. Geochim. Cosmochim. Acta 70, 1668–1676.

Willbold, M., Elliott, T., Moorbath, S., 2011. The tungsten isotopic composition of the Earth's mantle before the terminal bombardment. Nature 477, 195–198.

Wimpenny, J., Gannoun, A., Burton, K.W., Widdowson, M., James, R.H., Gíslason, S.R., 2007. Rhenium and osmium isotope and elemental behaviour accompanying laterite formation in the Deccan region of India. Earth Planet. Sci. Lett. 261, 239–258.

Xing, Y., Brugger, J., Tomkins, A., Shavrov, Y., 2019. Arsenic evolution as a tool for understanding formation of pyritic gold ores. Geology 47, 335–338.

Zhong, R., Brugger, J., Tomkins, A.G., Chen, Y., Li, W., 2015. Fate of gold and base metals during metamorphic devolatilization of a pelite. Geochim. Cosmochim. Acta.

Zhu, W., Young, L.Y., Yee, N., Serfes, M., Rhine, E.D., Reinfelder, J.R., 2008. Sulfide-driven arsenic mobilization from arsenopyrite and black shale pyrite. Geochim. Cosmochim. Acta 72, 5243–5250.